Floquet engineering of dressed surface plasmon polariton modes in plasmonic waveguides

Kosala Herath [*] and Malin Premaratne [†]

Advanced Computing and Simulation Laboratory (AχL), Department of Electrical and Computer Systems Engineering, Monash University, Clayton, Victoria 3800, Australia

(Received 10 March 2022; revised 30 October 2022; accepted 5 December 2022; published 20 December 2022)

We present a comprehensive study surface plasmon polariton (SPP) propagation on planar metallic waveguides under a dressing field. We perform a set of analytical calculations of the periodic time-dependent Schrödinger equation to study the interaction of an intense electromagnetic field with a metallic system. We model the strong light coupling to the metallic system using a nonperturbative procedure. In this paper, we show that, by introducing Floquet theory into the dressed metal, the behavior of the Floquet states are similar to the phase-modulated signals in the communication system. This will reveal a new perspective on the underlying science in an intricate, dressed quantum system. Furthermore, we examine the impurity scattering effects on charge transport in disordered plasmonic metals using the generalized Floquet-Fermi golden rule and provide a novel approach to diminish the losses in plasmonic materials using the dressing field. To gauge the effectiveness of our results, we introduce a figure of merit to compare the performance of plasmonic metals, subjective to a dressing field. The calculated dressed SPP characteristics suggest that high-efficiency SPP propagation can be achieved in practice. Our findings open up new directions for state-of-the-art nanoplasmonic devices.

DOI: 10.1103/PhysRevB.106.235422

I. INTRODUCTION

We have witnessed an ever-increasing demand for faster information sharing and data processing capabilities over the last few decades. As a result, the semiconductor industry progresses towards faster, smaller, and more power-efficient semiconductor devices, circuits, and components. Nevertheless, signal delaying and thermal issues associated with electronic interconnections limit the continuous increase of data processing capacity in modern electronic devices. One of the most promising solutions introduced is substituting the electronic signals with optical waves for the reason that optical interconnections possess a significant information-carrying capability, low loss, and offers alternative methods to avoid the issues mentioned above [1–3]. However, the poor miniaturization capability of dielectric photonic devices leads to a significant size mismatch between modern electronic and photonic components. This prevents the implementation of light waves as data carriers in modern computing units [1]. The cause behind the constraint on the miniaturization of conventional photonic devices is the fundamental law of diffraction limit, i.e., an optical wave in a dielectric media cannot localize into nanoscale regions much smaller than the wavelength of the optical wave in the material [4]. An exciting area of research known as plasmonics has emerged to bridge this gap between microscale photonics and nanoscale electronics [5–7].

Plasmonics is a novel technology that studies the unique optical properties of metallic nanostructures to manipulate the propagation, localization, and guidance of light at the nanoscale [6]. Plasmonics, in principle, is concerned with the behavior of plasmons. Plasmon is a quantum quasiparticle that represents a quantum of charge density oscillation. Researchers introduced two distinct concepts of plasmons (bulk and surface) to explain the two characteristic peaks in empirical observations on loss spectra [8–13]. Plasmon waves that occur independently in the volume of metal are described as *bulk plasmons* and are responsible for the high-frequency peak in the loss spectra. The lower-frequency peak on the loss spectra is due to the surface plasmons (SPs). In this article, we focus on the characteristics of SPs. SPs are plasmon waves that exist on the surface of a metal. Due to the collective oscillations of free electrons of the metal, SPs always arise with trapped electromagnetic fields on the surface. The combination of the surface charge oscillation and the linked electromagnetic field is called either a localized surface plasmon (LSP) for a closed surface of a small volume or a surface plasmon polariton (SPP) for an extended planar surface.

Various types of metallic nanostructures were proposed and analyzed for their LSP modes over the last few decades. These include spheres [14,15], hemispheres [16,17], ellipsoids [18,19], nanoshells [20,21], cubes [22,23], nanorods [24–26], and composite structures [27,28] formed by integrating basic shapes as building blocks. However, the most relevant mechanism required for concentrating and delivering light energy between nanophotonic devices is the guiding of SPPs. By changing the waveguide geometry, the characteristics of SPPs can be modified and this paves the path to unleash the full potential of nanophotonic devices. Thus, numerous geometrical nanostructures were investigated including thin metal films [29–31], cylindrical waveguides of

[*] kosala.herath@monash.edu
[†] malin.premaratne@monash.edu

a circular cross-section [32,33], cylindrical waveguides of a rectangle cross-section [34,35], gap waveguides [36,37], metal wedges [38–40], and arrayed nanoparticles [41–43]. With the recognition of the vast potential of SPPs, a wide range of novel applications originated in recent times, such as biosensors [44,45], optical devices [7,46–50], data storage [51,52], and photovoltaic devices [53,54]. Interestingly, the quality of the SPP waveguiding mechanism relies on two major factors: (i) propagation length and (ii) mode confinement [13]. Unfortunately, we cannot realize these two factors at the same time. The long-range SPP modes exhibit poor subwavelength field confinement while the short-range SPP modes provide better localization. With the possibility of strong subwavelength field confinement of the guided optical signals, highly integrated photonic circuits and nanophotonic technologies use the short-range SPP modes in most cases [1]. However, several critical issues prevent the realization of the immense potential of SPP-based future photonics, especially the propagation length limitations imposed by the inevitable propagation losses. The key to achieving a higher propagation length in plasmonic waveguides is reducing losses in the metal regions. One solution to compose a less-energy loss waveguide is to keep the majority of the field distribution away from the metal. We can achieve this by varying the geometrical parameters of the plasmonic waveguide [13,55–58]. Alternatively, we can use active waveguiding techniques to provide loss-compensating energy through electron or optical illumination [59–61]. Furthermore, several studies used the plasmonic laser or spaser (surface plasmon amplification by stimulated emission of radiation) [62,63] concept to build ultrafast nanoamplifiers for SPP waves [64,65]. However, a multitude of factors like the waveguide geometry, the operating frequency, and the nature of the implementation restricts the amount of energy that can be transferred to the SPP signal. In this paper, we present a novel analytical method to suppress energy losses and secure higher propagation length in plasmonic waveguides using Floquet engineering [66].

Identifying novel states of matter using controllable quantum systems has been under the spotlight of scientists over the past several decades. Researchers examine two main approaches to reach this goal. The first method is fabricating materials, or artificial materials [67,68]. The second method involves driving a system using external electromagnetic fields [66,69–71]. Since the driving mechanisms might enable us to explore unreachable conditions in static fabricated systems [71], driven quantum systems are a much better option to achieve unique states of matter. A better understanding of the fundamental mechanisms of charge transport in matter allows us to realize the SPP characteristics under an external field correctly. Most works studying the subject considered the driving field as a perturbation field [72,73]. Modeling the effects induced by external fields under a perturbative approach involves expanding the interaction terms in powers of the field intensity and discarding the higher-order terms. We can approximate the external field influence under the conventional perturbation approach in weak-intensity conditions. However, higher-order terms influence the physics at high intensities more strongly. This breaks the basis of the perturbative treatment. In these instances, a more accurate treatment needs to be adopted. A recent study by Wackerl *et al.* [74] derived a fully closed analytical expression for conductivity in a driven quantum system. In their theoretical and numerical analysis, they showed that the previous conventional perturbation approach based on results overestimated the driving field's effect on the transport properties. Formally, the driven-induced gauge fields generate an effective Hamiltonian that captures the unique characteristics of the driven quantum system. Our method deals with this effective time-dependent effective Hamiltonian. This allows us to identify exact solutions within the framework of the time-dependent Schödinger equation. Although the conventional perturbation approaches are valid under weak-intensity fields, our method can model the characteristics of the driven quantum system under any intensity range. In this study, we apply the Floquet engineering methods to find exact solutions for a driven quantum system. Floquet engineering is a unique procedure that manipulates quantum systems with a high-intensity time-periodic external electromagnetic field. This allows us to identify the SPP characteristics more accurately in any driving field's intensity range. At high intensities, we must treat the material and the radiation as a single combined quantum system, namely, a *dressed system*. We call the applied high-intensity radiation the *dressing field*. Under the Floquet engineering methods, we can dynamically generate fascinating exotic quantum properties by choosing a matching dressing field for the target material [66]. Theoretical analyses on the usage of Floquet engineering can be found in several fields of physics [66,70,71,74–76]. However, a detailed analysis of its application on plasmonic waveguides to manipulate SPP modes is still to be investigated in detail. Thus, this paper presents a robust theoretical analysis of dressed SPP modes in plasmonic waveguides.

In this study, we analytically examine the manipulation of SPP properties using a dressing field. First, we describe the behavior of electrons in a metal film under a dressing field with the help of the Floquet theory [70,77,78]. Then, we derive the Floquet-Fermi golden rule for the dressed metallic system. Here, we use a novel set of Green's functions, namely, the four-times Green's functions introduced in Ref. [74]. This leads to an analytical expression for the inverse scattering time of dressed electrons in the metal. Furthermore, we present an analytical mechanism to manipulate inverse scattering time through the intensity of the dressing field. Since the scattering rate and the inverse scattering time depend on the wave-function solutions, we can control the inverse scattering time by altering the electron wave functions. As long as the wave-function solution in a quantum Floquet system relies on the radiation strength, this will enable the possibility to tailor the transport properties and SPP properties using external radiation. In particular, we demonstrate that we can increase the propagation length of SPP modes in simple planner metal plasmonic waveguides. Finally, we use detailed numerical calculations to analyze the SPP properties of different plasmonic metals: silver (Au), gold (Au), copper (Cu), and aluminum (Al) under a dressing field.

One of the key results of our work is the comparison of various plasmonic metals under a dressing field. We introduce a new figure of merit (FoM) to evaluate the SPP characteristic improvements induced by the external dressing field. We can use this novel FoM formula to calculate the FoM values

of dressed plasmonic metals and compare their reliability in various plasmonic applications. Furthermore, we suggest several candidate plasmonic metals to be utilized when using our proposed method. This will pave the path to achieving high-efficiency state-of-the-art nanoscale plasmonic devices, circuits, and components.

Moreover, we believe that our theoretical model will initiate a specific experimental regime in SPP waveguides. As a direct result of our proposed mechanism, we can experimentally realize our prediction of the SPP propagation length enhancements with an external field. Due to its generality, the presented model can describe the experimental results taken from a broad class of materials and compare their deviations. Here, we modeled the influence of disorder structure in the metal as a single short-range perturbation potential. Analyzing the transport properties of a particular impurity distribution is a rather formidable task. In addition, we do not consider a specific impurity configuration in our study as it is unlikely to represent a measured impurity configuration in an experiment. Since we only assume elastic scattering arising from the impurities under our model, we can accurately describe systems with dominant elastic scattering. This can always be assumed if the temperature is low enough and photon absorption is restricted. To avoid the photon exchange between a driving field and conduction electrons, the radiation should be purely dressing. Our work gets inspiration from many similar studies [73,74,79,80] that used steady-state particle distribution function assumption with very low-temperature conditions. In those studies, the theoretical models are built on the free electron gas framework. A vital recurring theme of these theory works is the low-temperature stable conditions for free electron gas. Also, the radiation field must dress the system to avoid photon exchange between a driving field and conduction electrons. The frequency of the dressing field is far from resonant electron frequencies to reduce the energy absorption between the conduction band and the valence band of the electron gas. Moreover, the wave frequency ω is high enough to satisfy the inequality $\omega\tau_0 \gg 1$. Here, τ_0 is the electron relaxation time in a natural electron gas. Therefore, the intraband absorption of energy from the driving field by conduction electrons is negligible under this condition. Very much like all the theories mentioned before, we adopt the free electron gas model for our work. It is important to note that our analytical explanation of dressed plasmons is valid for any material that satisfies the free electron model conditions. We used Ag, Au, Cu, and Al metals to finally interpret our results as they are popular metals that meet the free electron model assumptions. In addition, we selected the dressing field's frequency in the same range that the authors of previous literature [80] used for their numerical calculations. This choice enables us to compare our analytical results with these earlier models. However, we may choose any material that satisfies the free electron gas model. In addition, to avoid the heating of the system, we can follow few other mechanisms to remove the heat from the interacting system and achieve a stable state. First, if we analyze our system under short timescales, then we can apply various approaches for stabilizing the driven quantum system using bath engineering methods [81–84]. With an upper limit for the dressing field's intensity, we can neglect the perturbative effects of the associated bath in the system. Next, we can use narrow pulses of a strong dressing field to avoid heating. This well-known methodology was elaborated upon long ago, and it is commonly used to observe various dressing effects—in particular, modifications of the energy spectrum of dressed electrons arising from the optical Stark effect—in semiconductor structures [80,85,86]. Finally, we restrict our dressing field intensity to a particular region under our model to eliminate the contribution from nonzero elements in the inverse scattering time matrix. In the experimental studies, we should identify the most promising regime for driven fields and materials to obey these validity settings.

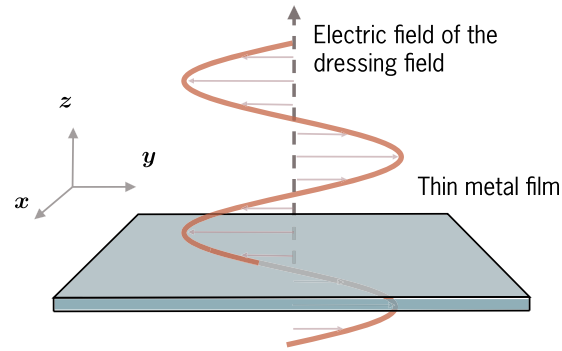

FIG. 1. Our thin metal film is placed in the xy-plane while the dressing field is applied perpendicular to the xy-plane. The dressing field is linearly polarized with a y-polarized electric field **E**.

The paper is organized as follows. Section II introduces our dressed metallic system and describes the electron behavior under the dressing field in the metal. Here, we employ the Floquet theory to describe the dressing field effects. Section III provides an analogy between Floquet states in dressed metallic systems and the phase-modulated signals in communication systems. We analyze the inverse scattering time for the dressed electrons in our metallic system using the Floquet-Fermi golden rule in Sec. IV. Section V presents a comprehensive numerical analysis of SPP characteristics under a dressing field. We propose a novel FoM value to evaluate plasmonic metals in Sec. VI. Section VII discusses the physical significance of our outcomes and their possible use in future nanoplasmonic devices. Finally, we summarize our findings and conclude our discussion in Sec. VIII. The derivation of the wave-function solutions for the dressed metallic quantum system is provided in Appendix A. Appendix B gives a detailed discussion on the metal disorder models. The derivation of the general Floquet-Fermi golden rule with t-t' formalism is given in Appendix C. We present the detailed numerical analysis of wavelength and decay lengths of dressed SPP modes in Appendix D.

II. FLOQUET THEORY PERSPECTIVE ON DRESSED METALS

SPPs only exist at a metal-dielectric interface. As an example we can generate SPPs in a surface of metal sheet in the air. Thus, it is necessary to analyze the behavior of electrons in a metal film under a dressing field. Therefore, we consider an isolated thin metal film subjected to an external high-intensity electromagnetic field as illustrated in Fig. 1. We

carefully select the frequency of the driving field to be in the off-resonant regime to avoid photon absorption and heating the system [81]. Therefore, the driving field behaves as a pure (nonabsorbable) dressing field.

Our analysis treats the fermion system and the radiation as one combined quantum system, namely, a dressed metal. We represent the metallic system with the free electron model. Under this model, we assume that a metal consists of electrons free to move in the crystal. Although the crystal lattice potential and electron-electron interactions are not explicitly taken into account, we can modify the model to overcome the deficiencies partly. In this modification, the electron mass m becomes an effective mass m_e [87]. In three-dimensional crystals, the electron acceleration will not be colinear. Thus, in general, we have an effective mass tensor. We consider the metals as isotropic mediums in the free electron model. Therefore, the conduction band electron's effective mass m_e becomes simply scalar.

A. Wave-function solutions for the dressed metal

Our system consists of a thin metal film placed on the xy-plane of the three-dimensional coordinate space. We consider a high-intensity linearly polarized electromagnetic field that propagates perpendicularly to the metal surface. In this study, we assume that the dressing field's wavelength is much larger than the height of the metal. Therefore, we can assume that the dressing field behaves as a homogeneous field inside the metal at a given time. In this study, we use linearly polarized radiation as the dressing field. Without any loss of generality, we can assume that the linearly polarized illumination possesses a y-polarized electric field $\mathbf{E}(t) = E\sin(\omega t)\hat{\mathbf{e}}_y$, where E is the amplitude of the electric field, ω is the frequency of the dressing field, and $\hat{\mathbf{e}}_j$ is the unit vector that is pointed to the subscript direction $j = x, y$. Furthermore, we can model the dressing field in the Coulomb gauge as a vector potential

$$\mathbf{A}(t) = \frac{E}{\omega}\cos(\omega t)\hat{\mathbf{e}}_y. \tag{1}$$

The wave function of a single electron $\psi(\mathbf{r}, t)$ in the metal under the dressing field satisfies the time-dependent Schrödinger equation

$$i\hbar\frac{d\psi(\mathbf{r}, t)}{dt} = \hat{H}_e(t)\psi(\mathbf{r}, t), \tag{2}$$

with the time-dependent Hamiltonian $\hat{H}_e(t)$. Here, $\hbar$ is the reduced Planck constant, and $\mathbf{r} = (x, y, z)^\intercal$ is the position vector in the three-dimensional coordinate space. Since the vector potential is independent of the position coordinates, we can identify the time-dependent Hamiltonian as

$$\hat{H}_e(t) = \frac{1}{2m_e}[-\hbar^2\nabla^2 + 2ie\hbar\mathbf{A}(t)\cdot\nabla + e^2\mathbf{A}(t)\cdot\mathbf{A}(t)], \tag{3}$$

where m_e is the effective electron mass of the metal, and e is the elementary charge.

Since the metal block has a finite size, the wave function of the dressed metal electron is quantized. Following the procedure in Appendix A, we derive multiple discrete solutions for the wave function in the time-dependent Schrödinger equation

$$\psi_{\mathbf{k}}(\mathbf{r}, t) = \frac{1}{\sqrt{\mathcal{V}}}\exp\left[-i\left(\frac{\tilde{\varepsilon}_k}{\hbar}t + \frac{e^2E^2}{4m_e\omega^2\hbar}t - \frac{ek_yE}{m_e\omega^2}\sin(\omega t) + \frac{e^2E^2}{8m_e\omega^3\hbar}\sin(2\omega t)\right) + i\mathbf{k}\cdot\mathbf{r}\right], \tag{4}$$

where $\mathcal{V}$ is the volume of the system, $\mathbf{k} = (k_x, k_y, k_z)^\intercal$ is the wave vector, $\tilde{\varepsilon}_k = \hbar^2k^2/2m_e$ is the quantized energy levels for a bare electron, and $k = |\mathbf{k}|$ with the quantized values

$$k = \pi\left[\frac{n_x^2}{L_x^2} + \frac{n_y^2}{L_y^2} + \frac{n_z^2}{L_z^2}\right]^{1/2} \quad \text{with} \quad n_x, n_y, n_z \in \mathbb{Z}^+. \tag{5}$$

We used L_i to represent the length of the system in the i-direction. Furthermore, the wave function of the dressed electron can be rewritten as follows:

$$\psi_{\mathbf{k}}(\mathbf{r}, t) = \chi(\mathbf{k}, t)\varphi_{\mathbf{k}}(\mathbf{r}), \tag{6}$$

where

$$\chi(\mathbf{k}, t) = \exp\left[-\frac{i}{\hbar}\left(\tilde{\varepsilon}_k t + \frac{e^2E^2}{4m_e\omega^2}t - \frac{e\hbar k_yE}{m_e\omega^2}\sin(\omega t) + \frac{e^2E^2}{8m_e\omega^3}\sin(2\omega t)\right)\right], \tag{7}$$

and

$$\varphi_{\mathbf{k}}(\mathbf{r}) = \frac{1}{\sqrt{\mathcal{V}}}\exp(i\mathbf{kr}). \tag{8}$$

In the absence of the dressing field ($E = 0$), the wave function of the dressed electron reduces to the wave function of the bare electron in a finite space

$$\psi_{\mathbf{k}}|_{E=0}(\mathbf{r}, t) = \exp\left(-i\frac{\tilde{\varepsilon}_k}{\hbar}t\right)\varphi_{\mathbf{k}}(\mathbf{r}). \tag{9}$$

B. Floquet modes and quasienergies

Next, we recognize the momentum space wave-function solutions using the Fourier transformation [88] on a finite region

$$\psi(\mathbf{k}, t) = \sqrt{\mathcal{V}}\exp\left[-\frac{i}{\hbar}\left(\tilde{\varepsilon}_k t + \frac{e^2E^2}{4m_e\omega^2}t - \frac{e\hbar k_yE}{m_e\omega^2}\sin(\omega t) + \frac{e^2E^2}{8m_e\omega^3}\sin(2\omega t)\right)\right]. \tag{10}$$

Using Floquet theory [70,78], we can separate the *quasienergies* and time-periodic *Floquet modes* from the wave functions. Recall that the Floquet theory yields a factorization of the time evolution into periodic and exponential parts. The latter involves the quasienergy values [70]. Thus, we factorize the wave function in Eq. (10) into a linearly time-dependent part and a periodic time-dependent part. Here, we identify the quasienergies as

$$\varepsilon_k = \tilde{\varepsilon}_k + \frac{e^2E^2}{4m_e\omega^2}, \tag{11}$$

and represent the Floquet modes with

$$\phi(\mathbf{k},t) = \sqrt{\mathcal{V}}\exp(-i[\zeta(2\gamma k_y)\sin(\omega t) + \zeta(\gamma^2/4)\sin(2\omega t)]), \tag{12}$$

where $\zeta(\eta) = \hbar\eta/2m_e\omega$, and $\gamma = -eE/\hbar\omega$. Thereupon, we present the wave-function solutions for our dressed system as *Floquet states*

$$\psi(\mathbf{k},t) = \exp\left(-i\frac{\varepsilon_k}{\hbar}t\right)\phi(\mathbf{k},t), \tag{13}$$

with identified quasienergies and Floquet modes for each quantized $\mathbf{k}$ values.

III. ANALOGY TO PHASE MODULATION

In the previous section, we demonstrated the Floquet theory perspective on dressed metals. We illustrate the analogy between Floquet states and phase-modulated signals in the communication theory in this section [89]. After that, we propose a method to manipulate the Floquet modes using the dressing field.

A. Fourier series components of Floquet modes

Since the identified Floquet modes are time-periodic functions, we can expand them using the Fourier series expansion. First, recall the Jacobi-Anger expansion [91]

$$e^{-iz\sin(\theta)} = \sum_{l=-\infty}^{\infty} J_l(z)e^{-il\theta}, \tag{14}$$

where $J_l(\cdot)$ are Bessel functions of the first kind with lth integer order. Using Eq. (14), we can reformulate Eq. (12) as

$$\begin{aligned}\phi(\mathbf{k},t) &= \sqrt{\mathcal{V}}\sum_{l'=-\infty}^{\infty}\sum_{l=-\infty}^{\infty} J_{l'}(\zeta(2\gamma k_y))J_l(\zeta(\gamma^2/4))e^{-i(l'+2l)\omega t} \\ &= \sqrt{\mathcal{V}}\sum_{n=-\infty}^{\infty}\sum_{l=-\infty}^{\infty} J_{n-2l}(\zeta(2\gamma k_y))J_l(\zeta(\gamma^2/4))e^{-in\omega t}.\end{aligned} \tag{15}$$

Here, we introduced a new integer parameter $n = l' + 2l$. Now, we derive the Fourier series expansion of the Floquet modes by analyzing the structure of the above expression

$$\phi(\mathbf{k},t) = \sqrt{\mathcal{V}}\sum_{n=-\infty}^{\infty} u_n(\mathbf{k})e^{-in\omega t}, \tag{16}$$

where

$$u_n(\mathbf{k}) = J_n(\zeta(2\gamma k_y), \zeta(\gamma^2/4)). \tag{17}$$

Here, we use the definition of the generalized Bessel function of integer order [91]

$$J_n(z_1,z_2) = \sum_{l=-\infty}^{\infty} J_{n-2l}(z_1)J_l(z_2). \tag{18}$$

B. Frequency domain analysis

Note that the derived Floquet states in Eq. (13) are similar to the phase-modulated continuous signals in communication systems [89]

$$\chi_{\mathrm{PM}}(t) = A_c\exp[-i\omega_c t - i\Delta\chi(t)], \tag{19}$$

where $\chi_{\mathrm{PM}}(t)$ is the phase-modulated signal dependent on time, A_c is the amplitude of the carrier signal, ω_c is the frequency of the carrier signal, Δ the phase modulation index, and $\chi(t)$ is the information signal. For a given $\mathbf{k}$ wave vector, comparing Eqs. (13) and (19), we can identify the analogies between parameters

$$A_c \leftrightarrow \sqrt{\mathcal{V}}, \tag{20}$$

$$\omega_c \leftrightarrow \frac{\varepsilon_k}{\hbar} = \frac{\hbar^2k^2}{2m_e} + \frac{e^2E^2}{4m_e\omega^2}, \tag{21}$$

$$\Delta\chi(t) \leftrightarrow \zeta(2\gamma k_y)\sin(\omega t) + \zeta(\gamma^2/4)\sin(2\omega t). \tag{22}$$

Note that the quasienergy operates as the carrier signal frequency from this observation. Further, we observe that the dressing field behaves as a phase-modulated information signal on the electron wave function. If we turn off the external dressing field, the terms on the right-hand side of Eq. (22) will disappear. This leads to the bare electron wave function. This is an analogy to a carrier signal without any information signal in communication systems. Furthermore, we can manipulate the γ value using the applied dressing field's intensity. This allows us to control the effects of the dressing field in the same manner as the phase modulation index. Thus, we can conclude that the dressing field influence acts the same way as an information signal affects on the phase-modulated signal in a communication system. Accordingly, we can achieve diverse behaviors of charge transport properties in metals by applying different dressing field configurations, mimicking telecommunication analogies.

Now, we analyze our Floquet states in the frequency domain to find more analogies with the phase-modulated signal. Note that we examine the Floquet states for a given $\mathbf{k}$ wave vector in this section. Using the previous Floquet mode expansion in Eq. (16), we expand our Floquet states as a Fourier series

$$\psi_{\mathbf{k}}(t) = \sqrt{\mathcal{V}}\sum_{n=-\infty}^{\infty} u_n(\mathbf{k})e^{-i(\omega_k+n\omega)t}, \tag{23}$$

where the quasienergy frequency

$$\omega_k = \frac{\hbar k^2}{2m_e} + \frac{e^2E^2}{4m_e\hbar\omega^2}. \tag{24}$$

From Eq. (23), we observe that the frequency spectrum consists of a quasienergy-frequency line plus with an infinite number of sideband lines at frequencies $\omega_k \pm n\omega$. While these lines are equally spaced by the dressing field's frequency ω, we note that this exhibits the same behavior as the phase-modulated signal's frequency spectrum in communication systems [89]. The relative amplitude of a line at $\omega_k \pm n\omega$ is given by $u_n(\mathbf{k})$. To visualize the effect from the dressing field on the frequency spectrum of our Floquet states, we illustrate each amplitude of Fourier components using empirical

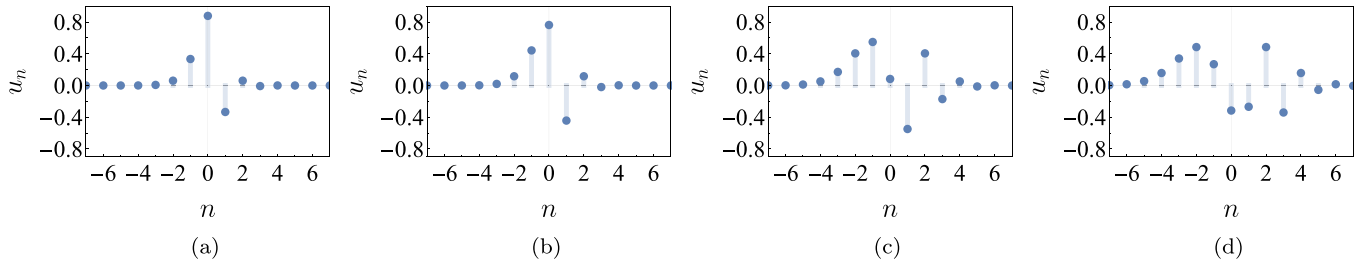

FIG. 2. The normalized Fourier components u_n of the Floquet states in dressed Ag for four distinct dressing field intensities (a) $I = 0.5I_0$, (b) $I = I_0$, (c) $I = 5I_0$, and (d) $I = 10I_0$ against the Fourier component number n. Here, $I_0 = 0.1\,\mathrm{W\,cm^{-2}}$, the dressing field frequency $\omega = 1.35 \times 10^{12}\,\mathrm{rads^{-1}}$, and $k_y = k_F^{\mathrm{Ag}}$. The empirical material parameters for Ag are used from Ref. [90] including effective mass $m_e^{\mathrm{Ag}} = 9.109 \times 10^{-31}$ kg, and Fermi wave vector $k_F^{\mathrm{Ag}} = 1.20 \times 10^{10}\ \mathrm{m^{-1}}$.

parameters [90] for Ag, one of the most common plasmonic metals. We demonstrate our results in Fig. 2, where we used four distinct dressing field intensity levels with the same dressing field frequency.

It can be observed from Fig. 2 that the number of nonzero components increase with the dressing field intensity. This suggests that we get multiple sidebands with a high-intensity field. Additionally, the relative amplitude of the sidebands varies with the dressing field's intensity. This behavior is identical to the frequency spectrum representation of phase-modulated signals in communication systems. A modulation index with a smaller magnitude implies a tight sideband structure and a larger magnitude implies an wide sideband structure. If $\Delta \ll 1$, then we assume that the spectrum consists of a carrier and two sideband lines. This is called the narrowband phase modulation (NBPM). However, if $\Delta \gg 1$, then multiple sideband lines will appear and produce a spectrum with a wide bandwidth. This modulation method is commonly known as wideband phase modulation (WBPM). In our case, we can identify the analogy of our system to NBPM or WBPM conditions. In a dressed metal system, these conditions are only defined by the applied electromagnetic field's amplitude. In other words, we need to address the contribution from multiple numbers of Floquet modes for a Floquet system under a high-intensity dressing field. Nevertheless, under low-intensity dressing field conditions, we can observe that the zeroth Floquet mode has the most significant contribution to charge transport properties. Thus, we can assume that the zeroth Floquet mode only induces the low-intensity dressing field effects.

As a result of the above-discussed similarities, we can adapt the information processing techniques from the communication systems to our dressed quantum systems. Thus, we predict that Floquet engineering will pave the way to introduce novel electronic and photonic applications in the future. As a feasible example, we can identify the intercavity modulation of the phase of the lasers, which is commonly known as frequency modulated (FM) laser oscillations [92,93]. Such modulations affect the properties of the emitted electromagnetic radiation, sometimes unpredictable at first sight [94]. In this mechanism, we can use an external high-intensity dressing field to manipualte the phase of the wavefunction of the electron in the cavity as discussed previously. Due to the periodic time dependence of parameters in the laser equation, any dressing field effect in the cavity can be decomposed as a superposition of Floquet solutions. With the help of previous analysis, we can expand these solutions as Floquet modes and their Fourier components. Using the understanding of these components, we can describe the underlying science of more complex time-dependent modulations to the laser equation. Thus, we believe that our theoretical analysis and knowledge generated from it will aid in the development of FM laser applications. However, these electronic and photonic applications require a rich physics treatment and need the contribution from multiple science and technology domains. As a starting point, we only consider the prospect of manipulating SPPs with the Floquet engineering methods in this study. Before proceeding with that, we need to analyze the inverse scattering time in dressed metals.

IV. INVERSE SCATTERING TIME ANALYSIS

In this study, we model metallic solids using the free electron model. Within the view of this model, we consider a gas of noninteracting electrons. Furthermore, we assume that the effective mass m_e takes the effects of band structure and electron-electron interactions into account [87]. Nevertheless, experimentally we can depict that the resistivity of a metal is inversely proportional to the temperature until it reaches a finite value [95]. This finite value (residual resistivity) is assumed to be generated by the imperfections in the crystal, such as impurities, vacancies, grain boundaries, or dislocations. The residual resistivity is essentially not temperature dependent. Additionally, the presence of impurity affects various electronic and photonic properties of metallic solids significantly. Theoretical understanding of the physical consequences caused by impurities in metal is critical from both fundamental and engineering perspectives. Furthermore, since we hope to interpret the low-temperature charge transport properties in metals, our free electron model needs an adjustment to address the ultracold electrical resistance. Therefore we introduce a static disorder potential $V(\mathbf{r})$ to our free electron model Hamiltonian to address this static impurities effects

$$\hat{H}_e(\mathbf{r}, t) = \frac{1}{2m_e}[\hat{\mathbf{p}} - e\mathbf{A}]\cdot[\hat{\mathbf{p}} - e\mathbf{A}] + V(\mathbf{r}). \tag{25}$$

This potential is also known as the *stationary scattering potential* of the system. In our analysis, we adopt the Gaussian

model with white noise conditions describing the disorder potential, and we extensively analyze this in Appendix B. We introduce a crucial parameter named inverse scattering time to address the charge transport modifications induced by the scattering potential.

A. Inverse scattering time matrix for dressed metals

Following the general Floquet-Fermi golden rule presented in Appendix C, we can derive the inverse scattering time matrix for our dressed metal system. Due to the fact that we can describe our natural metallic system using a single energy band, we can neglect the energy band quantum numbers in the general Floquet-Fermi golden rule. Therefore, we can rewrite the inverse scattering time matrix for a given dressed metal as

$$\left(\frac{1}{\tau(\varepsilon,\mathbf{k})}\right)^{nn'} = \frac{2\pi V_{\text{imp}}}{\hbar}\frac{\mathcal{V}^2}{\mathcal{V}_{\mathbf{k}'}} \times \sum_{\mathbf{k}'} c_n(\mathbf{k},\mathbf{k}')[c_{n'}(\mathbf{k},\mathbf{k}')]^*\delta[\varepsilon-\varepsilon(\mathbf{k}')], \tag{26}$$

where

$$c_n(\mathbf{k},\mathbf{k}') = \sum_{m=-\infty}^{\infty} u_m(\mathbf{k})[u_{m+n}(\mathbf{k}')]^*. \tag{27}$$

Here, ε is a given energy value, $\mathcal{V}_{\mathbf{k}'}$ is the momentum space volume, $V_{\text{imp}} = \langle|V_{\mathbf{k},\mathbf{k}'}|^2\rangle_{\text{imp}}$ with $V_{\mathbf{k},\mathbf{k}'} = \langle\mathbf{k}|\upsilon(x)|\mathbf{k}'\rangle$, and $|\mathbf{k}\rangle$ is a bare electron state with $\mathbf{k}$ momentum. $\langle\cdot\rangle_{\text{imp}}$ presents the average over realizations of the impurity disorder.

Since the disorder is not supposed to change the eigenenergies of the undressed system [74], we can neglect the off-diagonal elements of the inverse scattering time matrix. Thus, we obtain the diagonalized inverse scattering time matrix for the dressed metal

$$\left(\frac{1}{\tau(\varepsilon,\mathbf{k})}\right)^{nn} = \frac{2\pi V_{\text{imp}}}{\hbar}\frac{\mathcal{V}^2}{\mathcal{V}_{\mathbf{k}'}}\sum_{\mathbf{k}'}|c_n(\mathbf{k},\mathbf{k}')|^2\delta[\varepsilon-\varepsilon(\mathbf{k}')]. \tag{28}$$

Substituting the Fourier components of Floquet modes presented in Eq. (17) back into Eq. (27), we find that

$$c_n(\mathbf{k},\mathbf{k}') = \sum_{m=-\infty}^{\infty} J_{n+m}(\zeta(2\gamma k_y'),\zeta(\gamma^2/4)) \times J_m(\zeta(2\gamma k_y),\zeta(\gamma^2/4)). \tag{29}$$

Using the generalized Neumann's addition theorem for the generalized Bessel functions [91]

$$\sum_{m=-\infty}^{\infty} J_{n\mp m}(z_1,z_2)J_m(z_1',z_2') = J_n(z_1\pm z_1', z_2\pm z_2'), \tag{30}$$

we evaluate the inverse scattering time matrix elements with the following expression:

$$\left(\frac{1}{\tau(\varepsilon,\mathbf{k})}\right)^{nn} = \frac{2\pi V_{\text{imp}}}{\hbar}\frac{\mathcal{V}^2}{\mathcal{V}_{\mathbf{k}'}} \times \sum_{\mathbf{k}'} J_n^2(\zeta[2\gamma(k_y-k_y')])\delta(\varepsilon-\varepsilon_{k'}). \tag{31}$$

By introducing the momentum continuum limit in polar coordinates, we can write Eq. (31) as

$$\left(\frac{1}{\tau(\varepsilon,\mathbf{k})}\right)^{nn} = \frac{V_{\text{imp}}\mathcal{V}^2}{4\pi^2\hbar}\int_0^{\infty}\int_0^{\pi}\int_0^{2\pi}\delta(\varepsilon-\varepsilon_{k'})k'^2\sin\theta' \times J_n^2(\zeta[2\gamma(k_y-k'\sin\theta'\sin\varphi')])d\varphi' d\theta' dk'. \tag{32}$$

We only focus on the electrons that possess energy near the Fermi energy under the charge transport analysis. Thus, we can simplify the above equation as

$$\left(\frac{1}{\tau(\varepsilon_F,\mathbf{k})}\right)^{nn} = \frac{V_{\text{imp}}\mathcal{V}^2}{4\pi^2\hbar}\int_0^{\infty}\int_0^{\pi}\int_0^{2\pi}\delta(\varepsilon_F-\varepsilon_{k'})k'^2\sin\theta' \times J_n^2\{\zeta[2\gamma(k_y-k'\sin\theta'\sin\varphi')]\}d\varphi' d\theta' dk'. \tag{33}$$

with

$$\varepsilon_F = \frac{\hbar^2}{2m_e}k_F^2, \tag{34}$$

where ε_F is the Fermi energy, and k_F is the Fermi wave vector. Then, we substitute the energy parameter to the momentum parameter k' in the integral using the definition of quasienergy after neglecting the constant shift of the energy added by the dressing field

$$\varepsilon_{k'} = \frac{\hbar^2}{2m_e}k'^2 \Rightarrow k'dk' = \frac{m_e}{\hbar^2}d\varepsilon_{k'}, \tag{35}$$

and Eq. (33) simplifies to

$$\left(\frac{1}{\tau(\varepsilon_F,\mathbf{k})}\right)^{nn} = \frac{m_e k_F V_{\text{imp}}\mathcal{V}^2}{4\pi^2\hbar^3}\int_0^{\pi}\int_0^{2\pi}\sin\theta' \times J_0^2(\xi[\kappa_y-\sin\theta'\sin\varphi'])d\varphi' d\theta', \tag{36}$$

where

$$\xi = \frac{eEk_F}{m\omega^2}, \quad \text{and} \quad \kappa_y = \frac{k_y}{k_F}. \tag{37}$$

B. Numerical analysis of energy band broadening

We define the normalized energy band broadening matrix elements as

$$\Gamma^{nn}(\varepsilon_F,\mathbf{k}) = \frac{[1/\tau(\varepsilon_F,\mathbf{k})]^{nn}}{[1/\tau(\varepsilon_F,\mathbf{k})]^{00}\big|_{E=0}}, \tag{38}$$

and we can evaluate this by

$$\Gamma^{nn}(\varepsilon_F,\mathbf{k}) = \frac{1}{4\pi}\int_0^{\pi}\int_0^{2\pi}\sin\theta' J_n^2(\xi[\kappa_y-\sin\theta'\sin\varphi'])d\varphi' d\theta'. \tag{39}$$

In this analysis, we are only interested in electrons that contain energy near the Fermi energy. Thus, we can derive that $|\mathbf{k}| \approx k_F$. Therefore, we can identify that $|k_y| \leqslant k_F$, and $|\kappa_y| \leqslant 1$. Under this condition, we numerically calculate the normalized energy band broadening against κ_y for several intensity levels of dressing field and the results are illustrated in Fig. 3. By comparing each diagonal element value in the subfigures of Fig. 3, we can identify that, when the value of n is moving away from the zero, normalized energy band broadening values reduce for each intensity level of the dressing field.

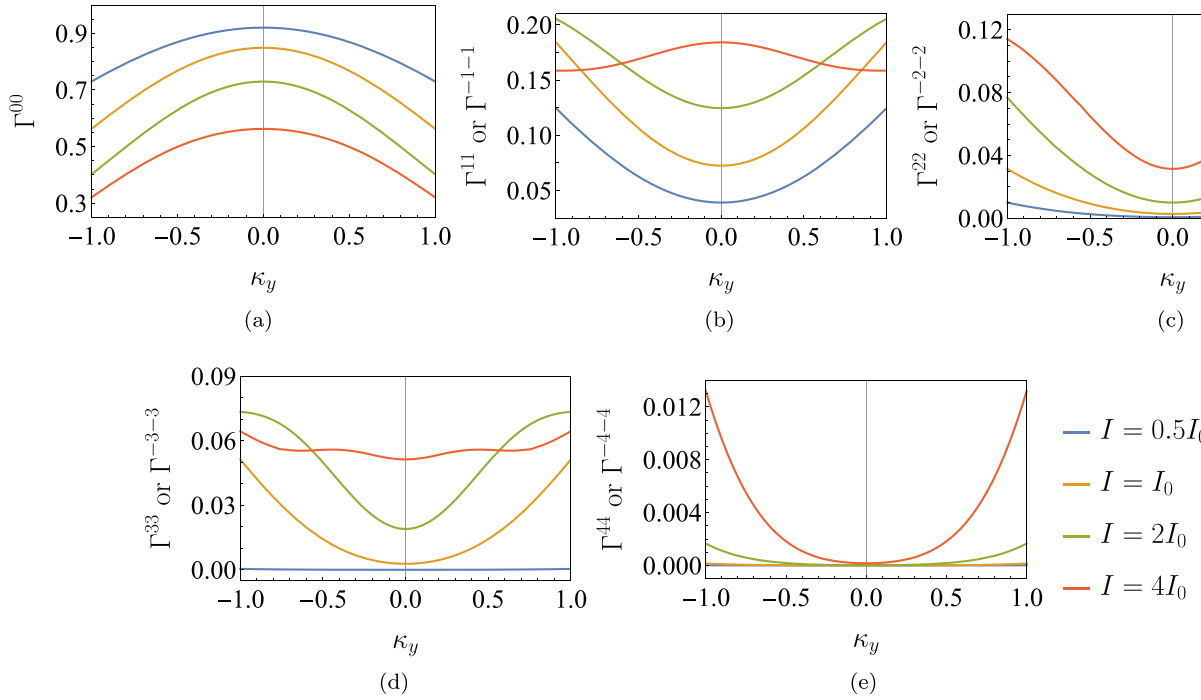

FIG. 3. The normalized inverse scattering time matrix diagonal elements in dressed Ag (a) Γ^{11} or Γ^{-1-1}, (b) Γ^{22} or Γ^{-2-2}, (c) Γ^{33} or Γ^{-3-3}, and (d) Γ^{44} or Γ^{-4-4} against the normalized y-directional wave-vector component κ_y with different intensities I of the external dressing field with a frequency of $\omega = 1.35 \times 10^{12}$ rads^{-1} and $I_0 = 0.1$ W cm^{-2}. The empirical material parameters for Ag are used from Ref. [90] including effective mass $m_e^{\mathrm{Ag}} = 9.109 \times 10^{-31}$ kg, and Fermi wave vector $k_F^{\mathrm{Ag}} = 1.20 \times 10^{10}$ m^{-1}.

Furthermore, the central element ($n = 0$) of the normalized energy band broadening matrix provides the largest contribution regardless of the intensity level. This implies that, under relative low-intensity fields, we can neglect the contribution of nonzero elements while analyzing the charge transport behaviors of dressed metals. However, the contribution from nonzero Floquet modes under high-intensity fields is significant. Thus, we need to address multiple nonzero diagonal elements from the inverse scattering time matrix. To make it more explicit, we illustrate normalized inverse scattering time matrix diagonal elements against the y-directional normalized wave vector in Fig. 4. Here, we use two distinct levels of intensities ($I = I_0$ and $I_0 = 16I_0$) for the dressing field. All diagonal elements show a general decrease with increasing the dressing field intensity. Under the low-intensity dressing field, we can neglect the contribution from nonzero diagonal elements compared to the central element of the normalized inverse scattering time matrix. However, the values of nonzero components are comparable to the central element value under the high-intensity field.

C. Normalized total energy band broadening

In this part of the analysis, we introduce an auxiliary parameter named normalized total energy band broadening (χ) for the conductivity electrons in the dressed metal. Under

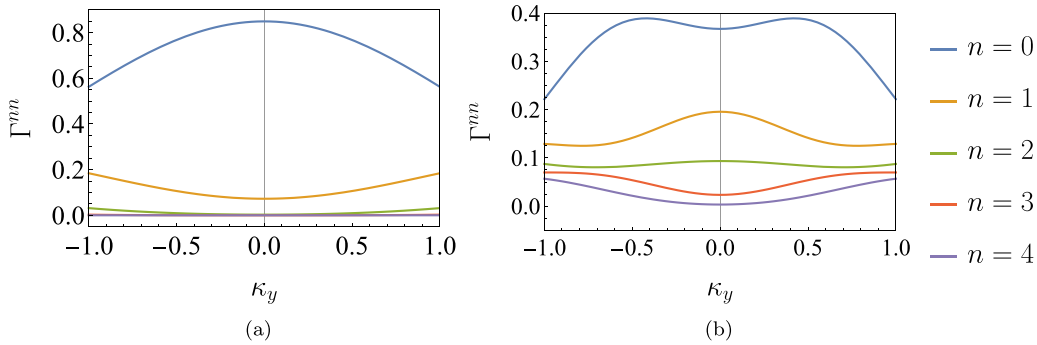

FIG. 4. The normalized inverse scattering time matrix diagonal elements Γ^{nn} in dressed Ag for two distinct dressing field intensities (a) $I = I_0$ and (b) $I = 16I_0$ against the normalized y-directional wave-vector component κ_y in a electron gas under dressing field with a frequency of $\omega = 1.35 \times 10^{12}$ rads^{-1} and $I_0 = 0.1$ W cm^{-2}. The empirical material parameters for Ag are used from Ref. [90] including effective mass $m_e^{\mathrm{Ag}} = 9.109 \times 10^{-31}$ kg and Fermi wave vector $k_F^{\mathrm{Ag}} = 1.20 \times 10^{10}$ m^{-1}.

low-intensity dressing field conditions, we only address the contribution from the central element ($n = 0$) of the inverse scattering time matrix for further analysis. First, we calculate the total energy band broadening ς of the conductivity electrons of dressed metal by

$$\varsigma = \frac{1}{V_{\mathbf{k}}} \sum_{V_{\mathbf{k}}} \left(\frac{1}{\tau(\varepsilon_F, \mathbf{k})} \right)^{00} \delta\left(\varepsilon_F - \frac{\hbar^2 k^2}{2m_e} \right). \tag{40}$$

Next, we evaluate ς by substituting the central element of the inverse scattering time matrix in Eq. (36) and introduce the momentum continuum limit in polar coordinates

$$\begin{aligned} \varsigma = \frac{1}{(2\pi)^3} \int_0^\infty \int_0^\pi \int_0^{2\pi} k^2 \sin\theta \frac{m_e k_F V_{\text{imp}} \mathcal{V}^2}{4\pi^2 \hbar^3} \\ \times \left[\int_0^\pi \int_0^{2\pi} \sin\theta' J_0^2(\xi[\kappa_y - \sin\theta' \sin\varphi']) d\varphi' d\theta' \right] \\ \times \delta\left(\varepsilon_F - \frac{\hbar^2 k^2}{2m_e} \right) d\varphi d\theta dk. \end{aligned} \tag{41}$$

Then, let $k_y = k \sin\varphi \sin\theta$ and this implies $\kappa_y = (k/k_F) \sin\varphi \sin\theta$. Now, ς can be expressed as

$$\begin{aligned} \varsigma = \frac{m_e k_F V_{\text{imp}} \mathcal{V}^2}{32\pi^5 \hbar^3} \int_0^\infty \int_0^\pi \int_0^{2\pi} k^2 \sin\theta \\ \times \left[\int_0^\pi \int_0^{2\pi} \sin\theta' J_0^2\left(\xi \left[\frac{k}{k_F} \sin\varphi \sin\theta \right.\right.\right. \\ \left.\left.\left. - \sin\theta' \sin\varphi' \right] \right) d\varphi' d\theta' \right] \delta\left(\varepsilon_F - \frac{\hbar^2 k^2}{2m_e} \right) d\varphi d\theta dk. \end{aligned} \tag{42}$$

We recall the energy parameter substitution in Eq. (35) and thus the above expression simplifies to

$$\begin{aligned} \varsigma = \frac{m_e^2 k_F^2 V_{\text{imp}} \mathcal{V}^2}{32\pi^5 \hbar^5} \int_0^\pi \int_0^{2\pi} \sin\theta \left[\int_0^\pi \int_0^{2\pi} \sin\theta' \right. \\ \left. \times J_0^2(\xi[\sin\varphi \sin\theta - \sin\theta' \sin\varphi']) d\varphi' d\theta' \right] d\varphi d\theta. \end{aligned} \tag{43}$$

By allowing $\xi = 0$, the natural energy broadening ς_0 of the metal can be written as

$$\varsigma_0 = \frac{m_e^2 k_F^2 V_{\text{imp}} \mathcal{V}^2}{32\pi^5 \hbar^5} \int_0^\pi \int_0^{2\pi} \sin\theta \left[\int_0^\pi \int_0^{2\pi} \sin\theta' d\varphi' d\theta' \right] d\varphi d\theta. \tag{44}$$

Next, we define the normalized total energy band broadening as

$$\chi = \frac{\varsigma}{\varsigma_0}, \tag{45}$$

and we obtain

$$\begin{aligned} \chi = \frac{1}{16\pi^2} \int_0^\pi \int_0^{2\pi} \sin\theta \left[\int_0^\pi \int_0^{2\pi} \sin\theta' \right. \\ \left. \times J_0^2(\xi[\sin\varphi \sin\theta - \sin\theta' \sin\varphi']) d\varphi' d\theta' \right] d\varphi d\theta. \end{aligned} \tag{46}$$

Moreover, we numerically calculate the relationship between the normalized total energy band broadening against the dressing field's intensity. Figure 5 demonstrates this relationship and we can identify that the normalized total energy band broadening reduces with increasing the applied dressing field's intensity. Here, all four metals show a general decrease in the total energy band broadening with increasing the intensity level of the dressing field while Al shows a relatively low-energy band broadening compared to other metals. It is important to note that we can interpret the total energy band broadening as the normalized damping factor for the electrons in the dressed metal system. Thus, we also refer to this parameter as $\chi = \varsigma/\varsigma_0$, with ς as the damping factor in the dressed metallic system, while ς_0 is the natural damping factor in the metallic system. This interpretation will help us to analyze the behavior of dressed SPPs in the next section.

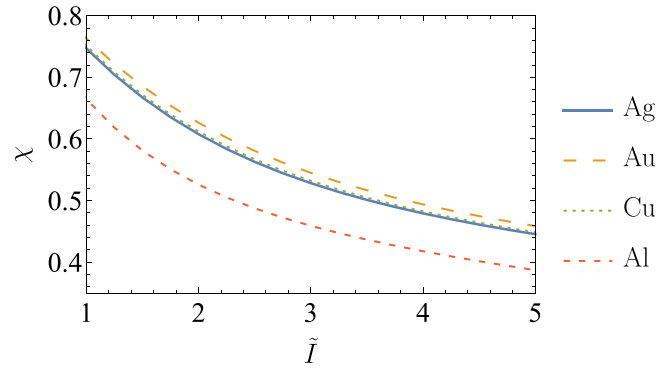

FIG. 5. The normalized energy band broadening χ against the normalized dressing field intensity $\tilde{I} = I/I_0$ for Ag, Au, Cu, and Al. Here, I is the dressing field intensity, $I_0 = 0.1\,\text{W cm}^{-2}$ and the dressing field's frequency is $\omega = 1.35 \times 10^{12}\,\text{rads}^{-1}$. The empirical material parameters for the metals are obtained from Refs. [90,96,97].

V. MANIPULATE SURFACE PLASMONIC POLARITONS

SPPs are collective oscillations in the electron charge density at the dielectric-metal interfaces. In this section, we examine a plane air-metal interface as illustrated in Fig. 6. The dielectric function of the air region ϵ_1 is assumed to be real, whereas the metal region ϵ_2 is characterized by a general, complex frequency-dependent dielectric function $\epsilon_2(\Omega) = \epsilon_2'(\Omega) + i\epsilon_2''(\Omega)$. Here, Ω is the angular frequency of the SPP excitation electromagnetic field. Since we model our metallic solid under the free electron model, we apply the Drude-Sommerfeld model [98,99] to derive expressions

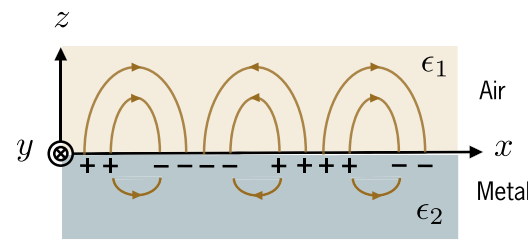

FIG. 6. The propagation of SPPs on the metal-air interface. Collective oscillations of electron charge density are positioned on the xy-plane, and the electric field lines of SPPs are illustrated on the xz-plane. The dielectric function of the air is ϵ_1 and the metal is ϵ_2.

for the real and imaginary components of the metal dielectric function

$$\epsilon_2'(\Omega) = 1 - \frac{\Omega_p^2}{\Omega^2 + \varsigma^2}, \tag{47}$$

$$\epsilon_2''(\Omega) = \frac{\varsigma \Omega_p^2}{\Omega(\Omega^2 + \varsigma^2)}, \tag{48}$$

where ς is the damping factor of the metal.

A. Characteristics of surface plasmonic polaritons

In general, we present the SPP's parallel wave number using a complex number $\varrho_x = \varrho_x' + i\varrho_x''$ where the real component ϱ_x' defines the SPP wavelength λ_{spp}, and the imaginary component ϱ_x'' describes the attenuation of the SPP while it travels along the interface. By solving the Maxwell's equations at the interface, we can write the dispersion equation for the SPP [98]

$$\varrho_x = \frac{\Omega}{c}\sqrt{\frac{\epsilon_1\epsilon_2}{\epsilon_1 + \epsilon_2}}, \tag{49}$$

where c is the speed of light in a vacuum. Considering the dielectric function of noble metals [100] with respect to the light wave frequencies, we can assume that $|\epsilon_2''| \ll |\epsilon_2'|$. Under this assumption, we derive expressions for the real and imaginary components of ϱ_x such that

$$\varrho_x' = \frac{\Omega}{c}\sqrt{\frac{\epsilon_1\epsilon_2'}{\epsilon_1 + \epsilon_2'}}, \tag{50}$$

$$\varrho_x'' = \frac{\Omega}{c}\left[\frac{\epsilon_1\epsilon_2''}{2\epsilon_2'(\epsilon_1 + \epsilon_2')}\right]\sqrt{\frac{\epsilon_1\epsilon_2'}{\epsilon_1 + \epsilon_2'}}. \tag{51}$$

Then, the SPP wavelength is given by

$$\lambda_{\text{spp}} = \frac{2\pi}{\varrho_x'} = \sqrt{\frac{\epsilon_1 + \epsilon_2'}{\epsilon_1\epsilon_2'}}\lambda, \tag{52}$$

where $\lambda = 2\pi c/\Omega$ is the wavelength of the excitation electromagnetic field in free space. Furthermore, we express the normal component of the wave vector by

$$\varrho_{z,j} = \frac{\Omega}{c}\sqrt{\frac{\epsilon_j^2}{\epsilon_1 + \epsilon_2}}, \tag{53}$$

where $j = 1, 2$ represents the upper and lower regions.

B. Numerical results

From Sec. IV, we identified that we can manipulate the damping factor of the electrons in the metallic systems using a dressing field. This implies that we obtained the potential to manipulate the real and imaginary components of the dielectric function of metals. In this part of the analysis, we numerically evaluate the tunability of SPPs characteristics with an external electromagnetic field. For the simplicity, we can assume that $\epsilon_1 \approx 1$ for the dielectric region throughout the calculations. Unless specified otherwise, the following parameters are used in the numerical calculations: the excitation field frequency $\Omega = 2.975 \times 10^{15}\,\text{rads}^{-1}$ and the dressing field frequency $\omega = 1.35 \times 10^{12}\,\text{rads}^{-1}$. The effective mass m_e are $1.0m_0$, $1.1m_0$, $1.3m_0$, and $1.4m_0$ [90,96], and the Fermi energies are 5.5 eV, 5.53 eV, 7 eV, and 11.7 eV [90] for Ag, Au, Cu, and Al, respectively. Here, m_0 presents the mass of an electron. The Drude model parameters, plasma frequencies, and natural damping factors are obtained from Ref. [97]. The full MATHEMATICA code for the numerical calculations is available in Ref. [101].

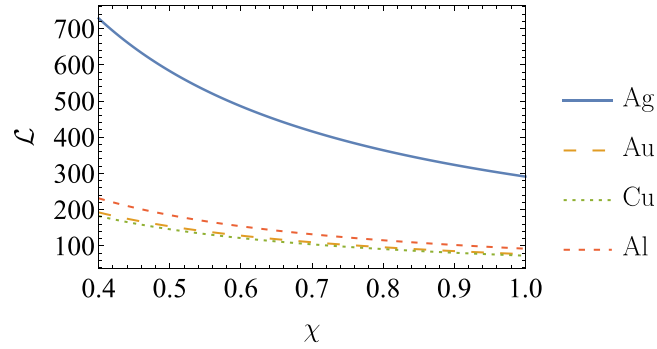

FIG. 7. The normalized propagation length $\mathcal{L}$ against normalized energy band broadening χ for Ag, Au, Cu, and Al. The empirical material parameters for the metals are obtained from Refs. [90,96,97].

The numerical evaluation of the dressing field effects on SPP wavelength and decay lengths reflects that the change in these characteristics is of the order of an angstrom in the best cases. Details of this numerical analysis can be found in Appendix D. Thus, we move our focus to the next significant property of SPPs. Here, we evaluate the potential to manipulate the propagation length of SPPs. We specify the propagation length of the SPP along with the interface by the imaginary part of the parallel wave number ϱ_x'' that is responsible for exponential attenuation of the electric field amplitude. We write the propagation length of the SPP as

$$L = \frac{1}{2\varrho_x''}. \tag{54}$$

Furthermore, we introduce the normalized propagation length concerning the wavelength of the excitation field and evaluate it as follows:

$$\mathcal{L} = \frac{L}{\lambda} = \frac{1}{2\pi}\left[\frac{\varepsilon_2'(1 + \varepsilon_2')}{\varepsilon_2''}\right]\sqrt{\frac{1 + \varepsilon_2'}{\varepsilon_2'}}. \tag{55}$$

Using the expressions in Eqs. (47) and (48), we can examine the relationship between the normalized propagation length and the normalized energy band broadening. This correlation for Ag, Au, Cu, and Al is depicted in Fig. 7. We can observe that the behavior of Au-based normalized SPP propagation length resembles those of Cu, and Al also shows almost similar behavior. However, the Ag-based curve shows a significant increase with decreasing the normalized energy band broadening. In other words, we can identify Ag-based SPP as an adequate candidate to achieve high-propagation lengths in plasmonic applications.

In general, we can observe that irradiating a metallic system with a dressing field increases the propagation length of SPP modes as a result of the metal's conductivity improvements. Surface plasmons result from collective oscillations of conduction electrons at the interface between a metal and

dielectric sustained by an electromagnetic wave. The electron charge density and its electromagnetic fields propagate as a surface wave along a metal-dielectric interface. Due to the propagation losses of conduction electrons, the electromagnetic field intensity decays exponentially away from the interface. The observation that the electrons lose energy in metals can be directly related to their scattering properties. Electron scattering is a fundamental physical mechanism consisting of the reflection of moving electrons in another direction. As a result, electron scattering causes the dissipation of the kinetic momentum of the electrons. Thus, we can use electron scattering to explain the reduced electron mobility in metals. There are various mechanisms of electron scattering in a metallic system, including elastic scattering processes generated by the disorders in metals and unelastic scattering processes caused by phonons. In our work, we assume that the temperature is always low enough to take that the elastic scattering is dominant in the conducting system. The presence of impurities and their elastic scattering cause residual electrical resistivity. The scattering amplitude or scattering rate indicates the amount of energy loss in the metal. Scattering rates generally depend on the details of the incident and outgoing state wave functions. Dressing by the external field modifies the wave functions and, thereby, the rates. This physical phenomenon was analyzed and used for many applications in previous literature [74,102–104]. By reducing the impurity-electron scattering rates, we can achieve higher electron mobility in a given direction. This leads to improved SPP propagation length in plasmonic waveguides. This physical description is summarized in Fig. 8. From the mathematical viewpoint, this can be explained by the rapid decrease of the Bessel function in Eq. (46) against the dressing field intensity. Focusing on the qualitative physical meaning of this behavior of SPP modes, we need to consider the characteristic changes in electron transport properties in dressed quantum systems. As was analytically explained in previous studies [73,74,76,79], we can achieve high-mobility rates and low-energy losses in electron transport by changing the natural electron states. By manipulating the wave-function solutions in the dressed SPP systems, we can decrease electron propagation losses in the metal region and enhance the propagation length of SPP modes. Since we adopt the more accurate Floquet engineering framework [74] to derive our analytical expressions, we believe our predictions will align better with the experimental observations.

Comparing the results from Appendix D and Fig. 7, we can identify that the changes impact on the propagation length of SPPs from a dressing field is noticeable compared to others. The ability to increase the propagation length of SPPs without altering other characteristics is a significant advancement in plasmonic devices. To make a comprehensive analysis, we examine the relationship between the normalized propagation length difference factor and the dressing field intensity. Here, we define the normalized propagation length difference factor as

$$\tilde{\mathcal{L}} = \frac{\mathcal{L} - \mathcal{L}|_{\chi=1}}{\mathcal{L}|_{\chi=1}}, \tag{56}$$

where $\mathcal{L}|_{\chi=1}$ is the natural normalized propagation length of SPP. Figure 9 depicts the behavior of the normalized

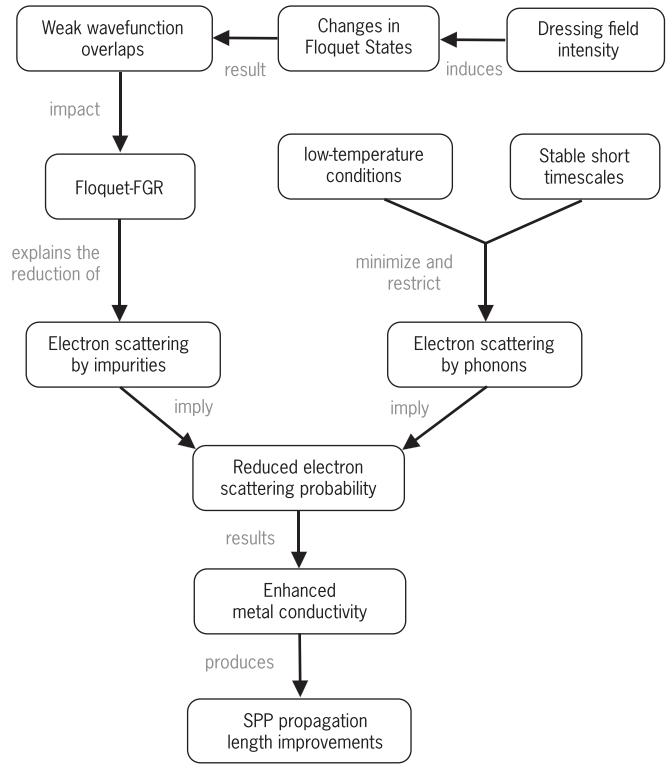

FIG. 8. A visual depiction of how the dressing field intensity affects conductivity and SPP propagation length. Here Floquet-FGR means the Floquet-Fermi's golden rule.

propagation length difference factor against the normalized dressing field intensity. All four metals show a positive-valued normalized propagation length difference factor. This signifies that we can enhance the propagation length of SPPs using an external dressing field. Significantly, the applied dressing field modifies the behavior of conducting electrons in the metal and this leads to SPPs with reduced losses inside the metal region. The curves of Ag, Au, and Cu show similar behavior against the changes of dressing field intensity. Nevertheless, Al shows a greater normalized propagation length enhancement than the other three metals. If we expect to find a good dressed plasmonic metal candidate for applications with increased efficiency, we need to compare the variations in all

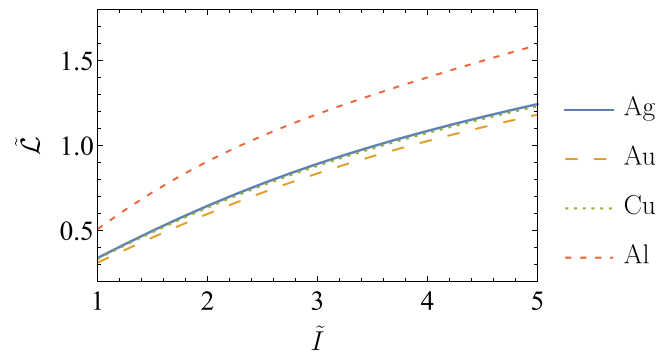

FIG. 9. The normalized propagation length $\tilde{\mathcal{L}}$ against normalized dressing field intensity $\tilde{I}$ for Ag, Au, Cu, and Al. The empirical material parameters for the metals are obtained from Refs. [90,96,97].

characteristics of SPP. Thus, in the next section, we introduce a new performance evaluation method to compare the dressed plasmonic metals.

VI. DRESSED SURFACE PLASMONIC POLARITON FIGURE OF MERIT

In practice, we can identify various SPP-based waveguide configurations along with different materials. Metal SPP-based waveguides offer specific advantages along with particular limitations. In the previous section, we propose a method to enhance the propagation length of SPPs by applying dressing radiation on the metal. Furthermore, we identify that different plasmonic metal waveguides behave differently variously against the dressing field. Thus, it is more convenient to propose a FoM that considers all the characteristics discussed previously. Then, we can use the FoM to assess the influence of the dressing field on different metals and select the best candidate out of different arrangements usable for a given application.

Ag and Au are noble metals and they are considered the material of choice for SPP waveguides due to the ease of implementation and stability against oxidation by the environment. Moreover, Cu and Al are also suitable for various plasmonic devices as their desirable properties and lower cost [105]. Due to high conductivity and inexpensiveness, Cu was used as a substitute for Ag and Au metals [106,107]. Since the potential of Al nanostructures to sustain surface plasmon resonances in the UV region, it was used in various optoelectronic applications [108,109]. Accordingly, we included these four metals under our evaluation of FoM.

There are several FoMs proposed in the literature to evaluate and compare the performance of SPPs [110–112]. However, the key point of this study is to evaluate the dressing field influence on SPP properties for each metal. This requires the FoMs to only assess the characteristics differences caused by the dressing field. Using the definitions given in Sec. V, we define the new FoM as

$$\mathrm{FoM} = \left| \frac{\tilde{\mathcal{L}}\tilde{\Delta}_2}{\tilde{\Delta}_1 \tilde{\Lambda}} \right|. \tag{57}$$

A higher FoM value indicates a better improvement of single metal SPPs over another under a dressing field.

The new FoM directly compares different plasmonic metals in terms of the four factors introduced previously. The first factor is $\tilde{\mathcal{L}}$ and it represents the propagation length enhancement as a normalized deviation factor. Since the higher values of $\tilde{\mathcal{L}}$ are favorable effects on the SPPs' propagation, we include it as a numerator in the FoM. We expect to compare the metal performance for utilizing them in plasmonic waveguides. Thus, it is better to confine the SPP into the interface. This requires a lower decay length in both regions. Under the dressing field $\tilde{\Delta}_1$ shows a raise while $\tilde{\Delta}_1$ declines. Consequently, we include the $\tilde{\Delta}_1$ and $\tilde{\Delta}_2$ as a denominator and numerator, respectively. In plasmonic applications, it is crucial to maintain the wavelength of the SPP. Thus, we expect a minimized dressing field effect on the wavelength of the SPP. As a result, we include the normalized propagation wavelength difference factor in the denominator of the FoM. Since we address the sign of these parameters by placing them in the FoM, we only need to consider the magnitude of these factors. Note that the FoM depends on the choice of the excitation frequency and the dressing field intensity.

TABLE I. FoM results for Ag, Au, Cu, and Al under two distinct dressing field intensities ($I = I_0$ and $I = 4I_0$). Here $I_0 = 0.1\,\mathrm{W\,cm^{-2}}$.

FoM (10^{-5})	$I = I_0$	$I = 4I_0$
Ag	2.5488	4.6941
Au	0.1858	0.3387
Cu	0.1795	0.3291
Al	0.1536	0.2861

Table I gives the new FoM values for all these four metals for two intensity levels of dressing field ($I = I_0$ and $I = 4I_0$). Here we use the same excitation frequency $\Omega = 2.975 \times 10^{15}\,\mathrm{rads^{-1}}$ as the previous calculations. The second and third columns show the FoM values for low and high dressing field intensity level, respectively. Under both conditions, we can arrange in the order of their FoM as Ag > Au > Cu > Al. The results show that the Ag-based SPPs outperforms the other three metals with significant variance. This describes its ability to achieve propagation length improvements while minimizing the variations in other characteristics. Furthermore, Cu and Au show almost similar results under the two intensity levels, while Al performs poorly. Thus, Al is not an attractive plasmonic material under these conditions. However, we can identify that this is due to the existence of interband transitions in the visible wavelength range and large values of $\epsilon''(\Omega)$. We can expect better results for Al in the high-frequency range excitation fields.

Every single application of surface plasmons suffers from damping caused by absorption in metals [113]. This results in propagation length limitations. Thus, finding a solution for this is a very hot topic in modern photonic research. One way of achieving high propagation lengths is an amplification of plasmons analogous to photon amplification in a laser [113,114]. For this, it is required to introduce an optical gain to the surrounded medium of the metallic structure [114]. Several remarkable research used this technique with optically pumping dye-impregnated polymers [113], semiconductor heterostructures [61,115], erbium-doped phosphate glass [116], and polymer embedded with quantum dots [117]. Under this technique, the gain required to match with the SPP losses, and it is significant [1]. Thus, this is a challenging process to achieve. On the other hand, one can achieve higher propagation lengths in SPPs by following passive approaches such as adopting different shapes and geometrical parameters [55,56,58]. However, the possible enhancement of the propagation length is limited, and the choice of geometrical parameters can be restricted by the application. Thus, we propose our approach of enhancing the SPP propagation length using an external dressing field as a replacement for the above techniques.

The realization of the improvements in propagation length of SPP promises its potential in advanced plasmonic applications. With our detailed analytical model, we demonstrate that it is possible to improve the propagation lengths in SPP

applications. Furthermore, we present a comprehensive comparison between metals as candidates for dressed SPPs. As a result, we identify that Ag-based SPPs outperformed under the dressing field influence. Thus, we suggest that Ag is a potential plasmonic material for achieving long-propagation lengths while maintaining other properties almost steady.

VII. PROSPECTS FOR APPLICATIONS

The SPP-based nanostructures demonstrate their strong subwavelength localization of SPP modes. This encourages the advancement of highly integrated and efficient plasmonic signal-processing components and devices. We can separate the present investigations and applications on SPP-based nanostructures into two interrelated areas: short-range SPPs with extreme confinement and long-range SPPs with reduced confinement. Under our proposed method, we hope to achieve higher propagation lengths while the mode confinement remains unchanged. Thus, this technique realizes long-range SPPs with higher electromagnetic wave confinement. We believe that this can be exploited in both areas of applications mentioned above.

Various experimental and theoretical techniques were proposed to realize high-efficiency plasmon waveguides. Zia *et al.* [118] introduced a method to develop plasmonic waveguides with metal stripes while channels built with periodically corrupted regions were suggested by Bozhevolnyi *et al.* [119]. Furthermore, several nanowaveguide formations [120] and gap waveguides with SPP propagation between profiled metal surfaces were proposed [121,122]. The main challenge in this field of application is to strongly confine the SPP wave while keeping relatively high propagation lengths [122]. A reduced SPP propagation length leads to low efficiency waveguiding [123]. Our analysis shows that we can enhance the propagation length using an external dressing field. Thus, our theoretical model will aid in the realization of high-efficiency plasmonic waveguides.

SPP-based optical lenses are one of the most important applications because they allow to couple a plane propagating wave to a spatially localized wave mode. In plasmonics, several methods were introduced for wave focusing by restructuring the surface of a metal film with curved slits [124], curved ridges [125], and a curved chain of nanoparticles [126]. Due to the short propagation length of SPP in these methods it gives a low-efficiency rate. As a solution, these methods can take advantage of our proposed methods to reduce the propagation losses and obtain relatively long propagation lengths.

Plasmonic sensing is a significant multidisciplinary research area. It has been largely employed in detecting trace molecules in chemistry and biology [127]. Nanowire-based SPPs are novel types of structures for sensing applications. The characteristics of nanowire SPP are susceptible to changes in the dielectric environment [128]. This results in them being used in sensing applications. Recently, several efforts were made to improve the efficiency of SPP-based sensors [127,129]. However, it is vital to remove ambiguity on the characteristics of SPP while applying improvements. Thus, we believe that our dressed SPP method would be a good candidate for improving the efficiency of plasmonic sensor applications.

By selecting a proper plasmonic metal as described in Sec. VI, we can specifically add modifications to the propagation length of dressed SPP modes. This will lead the way to innovate novel optically controlled SPPs-based switching devices. Since the basic components of modern electronics are switching devices, we expect that our proposed methods and detailed numerical analysis will aid in the advances in the future nanoscale electronics and photonic devices.

Investigation of low-dimensional SPPs characteristics is one of the major emerging research area in the last decade due to their feasibility in modern applications. However, the SPPs in two-dimensional systems can no longer be described in relation to the bulk SPPs and requires a different analytical model [130]. We believe that applying an external dressing field will improve the propagation length of SPPs in low-dimensional systems as well. To derive an analytical expression to describe the properties of dressed two-dimensional (2D) SPPs through our proposed analytical model needs to be reformulated from the beginning. However, consideration of dressed SPPs in low-dimensional systems will offer further directions for extensions and might reveal new, interesting physics.

VIII. CONCLUSION

We studied the behavior of electrons in a periodically driven metallic system under the free electron model assumptions. With the help of the Floquet theory, we demonstrated that we could present the nonperturbative solution of electron wave functions as Floquet states. Then, we derived an analytical expression for the total energy band broadening of the metallic system under the dressing field using the Floquet-Fermi golden rule. Here, we assumed that the driving field only renormalizes the Floquet system's parameters rather than changing the particle distribution under low temperatures. Since there is a novel regime of closed Floquet systems with a quasi-steady-state that persists for a considerably long time, it is a reasonable assumption that the particle distribution is time independent.

Using our derived expression for the total energy band broadening, we found that the system's scattering rate or the energy band broadening depends on the Floquet states. As long as the wave-function solution in a quantum Floquet system depends on the dressing field's intensity, this will enable the possibility to tailor the transport properties using external radiation. This implies that we could manipulate the SPP properties as well. Primarily, we found that the dressing field enhances the propagation length of the SPP mode while the modifications made on the other characteristics are relatively low. Furthermore, we presented a novel FoM to evaluate the improvements added by the dressing field on the plasmonic metal. We used the proposed FoM to compare various modifications on noble, transition, and posttransition metals using Ag, Au, Cu, and Al as the representative plasmonic materials. Using the evaluated values of FoM, we suggested Ag as a better candidate to achieve SPP with long propagation lengths while other properties remained roughly unaffected.

The realization of intrinsic challenges in identifying the optimum SPP components in plasmonic devices alleviates the burden of advancing the efficiency of SPP applications and makes future research clear and innovative. The formalism and intuitive understanding presented in this paper can be used to enhance the efficiency of a variety of plasmonic systems under the application of a dressing field. The demonstrated ability of the enhanced SPP propagation initiates new horizons in the advancement of different applications of nanoplasmonics.

We leave some important generalizations for future work. Recent literature introduced novel analytical concepts on the Floquet-Hamiltonian that correctly described heating dynamics [131,132]. Although our results were obtained on short timescales, related studies suggested that dissipation due to interparticle collisions could lead to heating in quantum Floquet systems under long timescale conditions. We are planning to use this generalized description to explain the dressed SPP characteristics in long timescales.

ACKNOWLEDGMENTS

K.H. wishes to acknowledge the members of AχL at Monash University for their encouragement and support. The work of K.H. is supported by the Australian Government Research Training Program (RTP) Scholarship and the Monash University Institute of Graduate Research.

APPENDIX A: SCHRÖDINGER PROBLEM FOR DRESSED METALS

In this Appendix, we derive wave-function solutions in position space $\psi(\mathbf{r},t)$ for the time-dependent Schrödinger equation expressed in Eq. (2). The exact solutions of relativistic time-dependent Schrödinger for an electron in an external radiation was first derived by Volkov [133]. The wave fucntion of the charged particle, called the Gordon-Volkov wave function has been extensively used in many applications such as ones that calculate ionization of atoms [134], scattering of the charged particle [135], and excitation in band-gap semiconductors [136]. In the following, the steps of the finding the Gordon-Volkov wave-function solution for Eq. (2) are similar to the ones applied in Refs. [79,137,138].

Referring to the nonradiation condition solutions for the free electron model [139], we express the Gordon-Volkov wave function as

$$\psi_{\mathbf{k}}(\mathbf{r},t)=\frac{1}{\sqrt{\mathcal{V}}}e^{i\mathbf{k}\cdot\mathbf{r}}e^{-i\Phi_{\mathbf{k}}(t)}, \tag{A1}$$

where $\mathbf{k}$ is the electron's wave vector, $\mathcal{V}$ is the volume of the metal block, and $\Phi_{\mathbf{k}}(t)$ is the time-dependent Volkov phase [138]. Here, this solution represents a wave traveling in the positive $\mathbf{r}$ direction and a corresponding wave traveling in the opposite direction as well. We can substitute the Eq. (A1) back into the Eq. (2) and obtain [140]

$$\Phi_{\mathbf{k}}(t)=\int_0^t \frac{\hbar}{2m_e}\mathbf{k}\cdot\mathbf{k}-\frac{e}{m_e}\mathbf{A}(t')\cdot\mathbf{k}+\frac{e^2}{2m_e\hbar}\mathbf{A}(t')\cdot\mathbf{A}(t')dt'. \tag{A2}$$

Then applying the vector potential defined in Eq. (1) into this equation yields

$$\Phi_{\mathbf{k}}(t)=\int_0^t \frac{\hbar k^2}{2m_e}-\frac{ek_yE}{m_e\omega}\cos(\omega t')+\frac{e^2E^2}{2m_e\omega^2\hbar}\cos^2(\omega t')dt', \tag{A3}$$

where $k=|\mathbf{k}|$. We can assume that the metallic system is an isotropic medium under the free electron model. Therefore, we can identify that $k=\sqrt{k_x^2+k_y^2+k_z^2}$ and k_i is the electron wave-vector component in the i-direction. Now, we can easily solve this equation by direct integration over time t. Here, without loss of generality, we assume that the dressing field is switched on at $t=0$, and $\Phi_{\mathbf{k}}(0)=0$. In addition, the upper boundary condition

$$\lim_{t\to\infty}\mathbf{A}(t)=0 \tag{A4}$$

is applied to the dressing field. Then, the solution for $\Phi_{\mathbf{k}}(t)$ can be found as

$$\Phi_{\mathbf{k}}(t)=\left[\frac{\hbar k^2}{2m_e}+\frac{e^2E^2}{4m_e\hbar\omega^2}\right]t-\frac{ek_yE}{m_e\omega^2}\sin(\omega t)+\frac{e^2E^2}{8m_e\hbar\omega^3}\sin(2\omega t). \tag{A5}$$

Here, the first dressing-field-dependent additional term is the ponderomotive energy. The second term is the time-dependent position displacement of the electron due to the dressing field, giving rise to the so-called quiver motion [141]. The last term is a time-dependant phase-shift induced by the dressing field. Due to finite volume restrictions, we can identify a quantized electron wave vector $\mathbf{k}$. This leads to a discrete number of solutions for the wave function. Finally, we obtain wave-function solutions for the time-dependent Schrödinger equation

$$\psi_{\mathbf{k}}(\mathbf{r},t)=\frac{1}{\sqrt{\mathcal{V}}}\exp\left[-i\left(\frac{\tilde{\varepsilon}_k}{\hbar}t+\frac{e^2E^2}{4m_e\omega^2\hbar}t-\frac{ek_yE}{m_e\omega^2}\sin(\omega t)+\frac{e^2E^2}{8m_e\omega^3\hbar}\sin(2\omega t)\right)+i\mathbf{k}\cdot\mathbf{r}\right], \tag{A6}$$

where $\tilde{\varepsilon}_k=\hbar^2k^2/2m_e$ is the quantized energy levels for a bare electron, and $k=|\mathbf{k}|$ with the quantized values

$$k=\pi\left[\frac{n_x^2}{L_x^2}+\frac{n_y^2}{L_y^2}+\frac{n_z^2}{L_z^2}\right]^{1/2}\quad\text{with}\quad n_x,n_y,n_z\in\mathbb{Z}^+. \tag{A7}$$

Here L_i is the length of the metal block in the i-direction. This well-known answer was used frequently in the literature [79,135,142]. With the previously defined dressing field's upper bound condition, after a significant time period this wave function goes to a familiar bare electron wave function

$$\lim_{t\to\infty}\psi_{\mathbf{k}}(\mathbf{r},t)=\frac{1}{\sqrt{\mathcal{V}}}e^{i\mathbf{k}\cdot\mathbf{r}}e^{-i\frac{\tilde{\varepsilon}_k}{\hbar}t}. \tag{A8}$$

APPENDIX B: MODEL OF DISORDER

Consider a dressed fermion system described by the Hamiltonian in Eq. (25). The causes of the disorder potential $V(\mathbf{r})$ are numerous and ambiguous. In a metallic solid, the

reasons would be dislocations, substitutional impurities, vacancies, grain boundaries, and so on [87]. Finding the electric and optical properties for a specific impurity configuration is a rather formidable task and is not desirable since it is unlikely to have exactly the calculated impurity configuration in an experiment. Hence, our interest is in the statistically averaged properties of metals over impurity configurations. The static disorder potential corresponds to the situation in which the electrons scatter elastically, in other words, no change of energy. In this study, we only consider the elastic scattering processes.

1. Gaussian model

Suppose that the static scattering potential $V(\mathbf{r})$ is a continuous and random function of position. We choose the zero of energy such that the average potential is zero $\langle V(\mathbf{r})\rangle_{\text{imp}} = 0$, where $\langle\cdot\rangle_{\text{imp}}$ presents the average over realizations of the impurity disorder. We can derive one particularly straightforward model by assuming that $V(\mathbf{r})$ is a Gaussian random potential that can be characterized by

$$\langle V(\mathbf{r})\rangle_{\text{imp}} = 0, \tag{B1}$$

$$\langle V(\mathbf{r})V(\mathbf{r}')\rangle_{\text{imp}} = \Theta(\mathbf{r}-\mathbf{r}'), \tag{B2}$$

where $\Theta(\mathbf{r}-\mathbf{r}')$ is a decaying function. Furthermore, we assume that it only depends on the distance $|\mathbf{r}-\mathbf{r}'|$ and that it decays with a characteristic length r_c.

In a scenario where the wavelength of radiation or scattered electrons is much greater than r_c, it is a reasonable approximation to take the two-point correlation function to be

$$\langle V(\mathbf{r})V(\mathbf{r}')\rangle_{\text{imp}} = \Upsilon\delta(\mathbf{r}-\mathbf{r}'), \tag{B3}$$

where the parameter Υ has dimensions of energy squared times volume. This implies that there is no spatial correlation. A random scattering potential $V(\mathbf{r})$ with this property is called a *white noise*.

2. Edwards model

The Gaussian model contains no information about the microscopic nature of disorder. Another model, introduced by Edwards [143], describes the potential $V(\mathbf{r})$ as the contribution of N_{imp} identical impurities in a volume $\mathcal{V}$, localized at randomly distributed points $\mathbf{r}_i$ and characterized by a potential $\upsilon(\mathbf{r})$

$$V(\mathbf{r}) = \sum_{i=1}^{N_{\text{imp}}} \upsilon(\mathbf{r}-\mathbf{r}_i). \tag{B4}$$

Furthermore, we take the limit $\mathcal{V}\to\infty$, while keeping the density $\eta_{\text{imp}} = N_{\text{imp}}/\mathcal{V}$ constant. The average distance between impurities is $\eta_{\text{imp}}^{-1/d}$ where d is the space dimensionality. Moreover, we assume that the $\upsilon(\mathbf{r})$ is a central potential, with a characteristic range r_0.

We can recover the Gaussian model by taking the limit of a high density ($\eta_{\text{imp}}\to\infty$) of weakly scattering impurities ($\upsilon(\mathbf{r})\to 0$) [87]. Furthermore, we can consider these single impurities as δ scatters

$$\upsilon(\mathbf{r}) = \upsilon_0\delta(\mathbf{r}), \tag{B5}$$

where υ_0 is a constant and this leads to

$$V(\mathbf{r}) = \sum_{i=1}^{N_{\text{imp}}} \upsilon_0\delta(\mathbf{r}-\mathbf{r}_i). \tag{B6}$$

When the disorders are evenly distributed over a large system, we can assume that the properties of the system can be described as an average over its ensemble of macroscopically identical subsystems [144]. This is also known as self-averaging. In this case, we can calculate the correlation function considering only a single impurity [87] as follows:

$$\langle V(\mathbf{r})V(\mathbf{r}')\rangle_{\text{imp}} = \eta_{\text{imp}}\int \upsilon(\mathbf{r}''-\mathbf{r})\upsilon(\mathbf{r}''-\mathbf{r}')d\mathbf{r}'', \tag{B7}$$

and this can be evaluated with

$$\langle V(\mathbf{r})V(\mathbf{r}')\rangle_{\text{imp}} = \eta_{\text{imp}}\int \upsilon_0^2\delta(\mathbf{r}''-\mathbf{r})\delta(\mathbf{r}''-\mathbf{r}')d\mathbf{r}''. \tag{B8}$$

Then we simply it into

$$\langle V(\mathbf{r})V(\mathbf{r}')\rangle_{\text{imp}} = \eta_{\text{imp}}\upsilon_0^2\delta(\mathbf{r}-\mathbf{r}'). \tag{B9}$$

By comparing Eq. (B9) with Eq. (B3), we can identify that

$$\Upsilon = \eta_{\text{imp}}\upsilon_0^2, \tag{B10}$$

and we can transform the Edwards model to the Gaussian model. In the framework of the Edwards model, this implies that the collisions are isotropic [87].

APPENDIX C: FOLQUET-FERMI GOLDEN RULE

We derive the Floquet-Fermi golden rule for a general dressed system with the help of the t-t' formalism. The steps of the derivation of the Fermi golden rule for t-t' Floquet states are similar to the one derived in Refs. [74]. We can identify the t-t'-Floquet states [70]

$$|\psi_\alpha(t,t')\rangle = \exp\left(-i\frac{\varepsilon_\alpha}{\hbar}t\right)|\phi_\alpha(t')\rangle, \tag{C1}$$

by separating the aperiodic and periodic components of the Floquet states. Here, α is the quantum number of the considering Floquet state. However, considering the properties of t-t'-Floquet states, we can find repeated Floquet states for each Floquet zone ($l = 0, \pm1, \pm2, \ldots,$) [70,74]. A general t-t'-state in the lth Floquet zone can be present as

$$\left|\psi_\alpha^l(t,t')\right\rangle = \exp[il\omega(t'-t)]|\psi_\alpha(t,t')\rangle. \tag{C2}$$

Furthermore, these states fulfill the t-t'-Schrödinger equation [70,74]

$$i\hbar\frac{\partial}{\partial t'}\left|\psi_\alpha^l(t,t')\right\rangle = \hat{H}_F(t')|\psi_\alpha^l(t,t')\rangle, \tag{C3}$$

where the *Floquet Hamiltonian* defined as

$$\hat{H}_F(t') = \hat{H}_e(t') - i\hbar\frac{\partial}{\partial t'}. \tag{C4}$$

Here, $\hat{H}_e(t)$ the time-dependent Hamiltonian of the dressed system. The corresponding time evolution operator to the t-t'-Schrödinger equation is given by

$$U_F(t,t_0;t') = \exp\left(-\frac{i}{\hbar}\hat{H}_F(t')[t-t_0]\right). \tag{C5}$$

It is important to note that the advantage of t-t' formalism lies on this time evolution operator that avoids any time-ordering operators [74].

As discussed in Appendix B, we model the stationary scattering potential by a group of randomly distributed impurities. We address this single scattering potential using the framework of the Edwards model with Gaussian white noise approximation. Furthermore, we assume that the perturbation was turned on at the reference time $t = t_0$. We modify our time-dependent Hamiltonian by adding a time-independent total perturbation $V(\mathbf{r})$.

$$i\hbar\frac{\partial}{\partial t'}\left|\Psi_\alpha^l(t,t')\right\rangle = [\hat{H}_F(t') + V(\mathbf{r})]\left|\Psi_\alpha^l(t,t')\right\rangle. \tag{C6}$$

This introduces a new wave-function solution $\langle\Psi_\alpha|$ for a system with a given perturbation. If $t \leqslant t_0$, both of the solutions for Eqs. (C3) and (C6) coincide

$$\left|\psi_\alpha^l(t,t')\right\rangle = \left|\Psi_\alpha^l(t,t')\right\rangle \quad \text{when} \quad t \leqslant t_0. \tag{C7}$$

Adopting the interaction picture representation [88,145], we write the t-t'-Floquet state as

$$\left|\Psi_\alpha^l(t,t')\right\rangle_I = U_0^\dagger(t,t_0;t')\left|\Psi_\alpha^l(t,t')\right\rangle. \tag{C8}$$

Due to time independence, the scattering potential has the same form in the interaction picture

$$V_I(\mathbf{r}) = U_0^\dagger(t,t_0;t')V(\mathbf{r})U_0(t,t_0;t') = V(\mathbf{r}). \tag{C9}$$

Now we can write the t-t'-Schrödinger equation in the interaction picture representation

$$i\hbar\frac{\partial}{\partial t'}\left|\Psi_\alpha^l(t,t')\right\rangle_I = V_I(\mathbf{r})\left|\Psi_\alpha^l(t,t')\right\rangle_I, \tag{C10}$$

with the recursive solutions [88,145]

$$\left|\Psi_\alpha^l(t,t')\right\rangle_I = \left|\Psi_\alpha^l(t_0,t')\right\rangle_I + \frac{1}{i\hbar}\int_{t_0}^{t} V_I(\mathbf{r})\left|\Psi_\alpha^l(t_1,t')\right\rangle_I dt_1. \tag{C11}$$

Next, we assume that the contribution from the higher-order terms of the perturbation can be neglected. Thus, we can write the solution up to the first-order term (Born approximation):

$$\left|\Psi_\alpha^l(t,t')\right\rangle_I \approx \left|\psi_\alpha^l(t_0,t')\right\rangle + \frac{1}{i\hbar}\int_{t_0}^{t} V_I(\mathbf{r})\left|\psi_\alpha^l(t_0,t')\right\rangle dt_1. \tag{C12}$$

Our general t-t'-Floquet states create a basis. Thus, we can write the solutions for the t-t'-Schrödinger equation given in Eq. (C10) employing our known t-t'-Floquet states

$$\left|\Psi_\alpha^l(t,t')\right\rangle = \sum_\beta a_{\alpha\beta}^{ll'}(t,t')\left|\psi_\beta^{l'}(t,t')\right\rangle. \tag{C13}$$

Here, we define the coefficient as the *scattering amplitude*

$$a_{\alpha\beta}^{ll'}(t,t') = \left\langle\psi_\beta^{l'}(t,t')\middle|\Psi_\alpha^l(t,t')\right\rangle, \tag{C14}$$

and we rewrite this as

$$a_{\alpha\beta}^{ll'}(t,t') = \left\langle\psi_\beta^{l'}(t,t')\middle|\psi_\alpha^l(t,t')\right\rangle + \frac{1}{i\hbar}\int_{t_0}^{t}\left\langle\psi_\beta^{l'}(t_1,t')\middle|V(\mathbf{r})\middle|\psi_\alpha^l(t_1,t')\right\rangle dt_1. \tag{C15}$$

Further, we examine a scattering phenomenon when a electron scatters from a known t-t'-Floquet state $|\psi_\beta^{l'}(t,t')\rangle$ into a distinct t-t'-Floquet state $|\Psi_\alpha^l(t,t')\rangle$ with a constant quansienergy ε as follows:

$$\psi_\beta^{l'}(\mathbf{k}',t,t') = e^{-\frac{i}{\hbar}[\varepsilon_\beta(\mathbf{k}')+l'\hbar\omega]t}\phi_\beta(\mathbf{k}',t')e^{il'\omega t'} \xrightarrow{\text{scattering}} \Psi_\alpha^l(\mathbf{k},t,t') = e^{-\frac{i}{\hbar}(\varepsilon+l\hbar\omega)t}\Phi_\alpha(\mathbf{k},t')e^{il\omega t'}. \tag{C16}$$

We calculate the scattering amplitude for this scattering scenario using the expression derived in Eq. (C15) as follows:

$$a_{\alpha\beta}^{ll'}(t,t') = \delta_{\alpha\beta}e^{i\omega(l-l')(t'-t)} + \frac{1}{i\hbar}\int_{t_0}^{t}\left\langle\psi_\beta^{l'}(t_1,t')\middle|V(\mathbf{r})\middle|\psi_\alpha^l(t_1,t')\right\rangle dt_1. \tag{C17}$$

Next, we write down the derived scattering amplitude as a Fourier series with second time argument (t')

$$a_{\alpha\beta}^{ll'}(t,t') = \sum_{n=-\infty}^{\infty} a_{\alpha,\beta}^{ll'}(t,n)e^{in\omega t'}, \tag{C18}$$

and we derive the these Fourier coefficients

$$a_{\alpha\beta}^{ll'}(t,n) = \frac{1}{T}\int_0^T a_{\alpha\beta}^{ll'}(t,t')e^{-in\omega t'}dt'. \tag{C19}$$

By subtituting the expression from Eq. (C17) into Eq. (C19), we obtain

$$a_{\alpha\beta}^{ll'}(t,n) = \delta_{\alpha\beta}\delta_{n,l-l'}e^{-in\omega t} + \frac{1}{i\hbar}\int_{t_0}^{t} e^{\frac{i}{\hbar}[\varepsilon_\beta-\varepsilon+(l-l')\hbar\omega]t_1} \times \sum_{m=-\infty}^{\infty}\left\langle u_\beta^{m+l'+n}\middle|V(\mathbf{r})\middle|u_\alpha^{m+l}\right\rangle dt_1. \tag{C20}$$

We set t_0 to zero and for different quantum numbers $\alpha \neq \beta$, we can simplify this into

$$a_{\alpha\beta}^{ll'}(t,n) = -\frac{i}{\hbar}\int_0^t e^{\frac{i}{\hbar}[\varepsilon_\beta-\varepsilon+(l-l')\hbar\omega]t_1} \times \sum_{m=-\infty}^{\infty}\left\langle u_\beta^{m+l'+n}\middle|V(\mathbf{r})\middle|u_\alpha^{m+l}\right\rangle dt_1. \tag{C21}$$

Then, we rewrite the integral with the substitution $t_1 = t_1 - t/2$ as follows:

$$a_{\alpha\beta}^{ll'}(t,n) = -\frac{i}{\hbar}e^{-\frac{i}{2\hbar}[\varepsilon_\beta-\varepsilon+(l-l')\hbar\omega]t} \times \int_{-t/2}^{t/2} e^{\frac{i}{\hbar}[\varepsilon_\beta-\varepsilon+(l-l')\hbar\omega]t_1} \times \sum_{m=-\infty}^{\infty}\left\langle u_\beta^{m+l'+n}\middle|V(\mathbf{r})\middle|u_\alpha^{m+l}\right\rangle dt_1. \tag{C22}$$

In a long-time limit, the integral turns into a delta distribution

$$\lim_{t\to\infty}\int_{-t/2}^{t/2} e^{\frac{i}{\hbar}\varepsilon t_1}dt_1 = 2\pi\hbar\delta(\varepsilon). \tag{C23}$$

Therefore, the expression in Eq. (C22) yields

$$a^{ll'}_{\alpha\beta}(t,n) = -2\pi i\delta(\varepsilon_\beta - \varepsilon + (l-l')\hbar\omega) \times \sum_{m=-\infty}^{\infty} \langle u^{m+l'+n}_\beta | V(\mathbf{r}) | u^{m+l}_\alpha \rangle. \tag{C24}$$

Using the completeness property of free electron eigenstates $|\mathbf{k}\rangle$, we can obtain

$$a^{ll'}_{\alpha\beta}(t,n) = -2\pi i \sum_{\mathbf{k}}\sum_{\mathbf{k}'} \delta(\varepsilon_\beta(\mathbf{k}') - \varepsilon + (l-l')\hbar\omega) \times \sum_{m=-\infty}^{\infty} \langle u^{m+l'+n}_\beta | \mathbf{k}' \rangle \langle \mathbf{k}' | V(\mathbf{r}) | \mathbf{k} \rangle \langle \mathbf{k} | u^{m+l}_\alpha \rangle, \tag{C25}$$

and for a given $\mathbf{k}$ and $\mathbf{k}'$ values we can identify the scattering amplitude as

$$a^{ll'}_{\alpha\beta}(\mathbf{k},\mathbf{k}',t,n) = -2\pi i V_{\mathbf{k},\mathbf{k}'}\delta(\varepsilon_\beta(\mathbf{k}') - \varepsilon + (l-l')\hbar\omega) \times \sum_{m=-\infty}^{\infty} \left[u^{m+l'+n}_\beta(\mathbf{k}')\right]^* u^{m+l}_\alpha(\mathbf{k}). \tag{C26}$$

Here, $V_{\mathbf{k},\mathbf{k}'} = \langle \mathbf{k}' | V(\mathbf{r}) | \mathbf{k} \rangle$. Define a new function

$$c^n_{\alpha\beta}(\mathbf{k},\mathbf{k}') = \sum_{m=-\infty}^{\infty} u^m_\alpha(\mathbf{k}) \left[u^{m+n}_\beta(\mathbf{k}')\right]^*, \tag{C27}$$

and we restructure the expression in Eq. (C26) as

$$a^{ll'}_{\alpha\beta}(\mathbf{k},\mathbf{k}',t,n) = -2\pi i V_{\mathbf{k},\mathbf{k}'}\delta[\varepsilon_\beta(\mathbf{k}') - \varepsilon + (l-l')\hbar\omega] c^{l-l'+n}_{\alpha\beta}(\mathbf{k},\mathbf{k}'). \tag{C28}$$

This leads to the definition of the transition probability matrix

$$\left[A^{ll'jj'}_{\alpha\beta}(\mathbf{k},\mathbf{k}')\right]_{n,n'} = \sum_\gamma a^{ll'}_{\alpha\gamma}(\mathbf{k},\mathbf{k}',t,n)\left[a^{jj'}_{\beta\gamma}(\mathbf{k},\mathbf{k}',t,n')\right]^*. \tag{C29}$$

Substitute the expression from Eq. (C28) back into the above equation

$$\left[A^{ll'jj'}_{\alpha\beta}(\mathbf{k},\mathbf{k}')\right]_{n,n'} = 4\pi^2 V^2_{\mathbf{k},\mathbf{k}'} \sum_\gamma c^{l-l'+n}_{\alpha\gamma}(\mathbf{k},\mathbf{k}')\left[c^{j-j'+n'}_{\beta\gamma}(\mathbf{k},\mathbf{k}')\right]^* \times \delta[\varepsilon_\gamma(\mathbf{k}') - \varepsilon + (l-l')\hbar\omega]\delta[\varepsilon_\gamma(\mathbf{k}') - \varepsilon + (j-j')\hbar\omega]. \tag{C30}$$

However, we choose the quasienergies ε and any other ε_i to be in the central Floquet zone such that

$$|\varepsilon - \varepsilon_i| < \hbar\omega. \tag{C31}$$

This simplifies our expression for transition probability matrix

$$\left[A^{ll'jj'}_{\alpha\beta}(\mathbf{k},\mathbf{k}')\right]_{n,n'} = 4\pi^2 V^2_{\mathbf{k},\mathbf{k}'} \sum_\gamma c^n_{\alpha\gamma}(\mathbf{k},\mathbf{k}')\left[c^{n'}_{\beta\gamma}(\mathbf{k},\mathbf{k}')\right]^* \delta^2[\varepsilon - \varepsilon_\gamma(\mathbf{k}')]. \tag{C32}$$

Then rewrite the square of the delta distribution using the following interpretation [79,80]:

$$\delta^2(\varepsilon) = \delta(\varepsilon)\delta(0) = \frac{\delta(\varepsilon)}{2\pi\hbar}\lim_{t\to\infty}\int_{-t/2}^{t/2} e^{\frac{i}{\hbar}0t'}dt' = \frac{\delta(\varepsilon)t}{2\pi\hbar}. \tag{C33}$$

Using this relation on Eq. (C32), we can perform the time derivative of each matrix elements. Then, we define the transition amplitude matrix as

$$\Gamma^{nn'}_{\alpha\beta}(\mathbf{k},\mathbf{k}') = \frac{d\left[A^{ll'jj'}_{\alpha\beta}(\mathbf{k},\mathbf{k}')\right]_{nn'}}{dt}, \tag{C34}$$

and we evaluate this as follows:

$$\Gamma^{nn'}_{\alpha\beta} = \frac{2\pi}{\hbar}V^2_{\mathbf{k},\mathbf{k}'}\sum_\gamma c^n_{\alpha\gamma}(\mathbf{k},\mathbf{k}')\left[c^{n'}_{\beta\gamma}(\mathbf{k},\mathbf{k}')\right]^*\delta[\varepsilon - \varepsilon_\gamma(\mathbf{k}')]. \tag{C35}$$

To calculate the inverse scattering time matrix, first we take the impurity average and then the sum over all momenta over the transition probability matrix

$$\left(\frac{1}{\tau(\varepsilon,\mathbf{k})}\right)^{nn'}_{\alpha\beta} = \frac{1}{\mathcal{V}_{\mathbf{k}'}}\sum_{\mathbf{k}'}\left\langle\Gamma^{nn'}_{\alpha\beta}(\mathbf{k},\mathbf{k}')\right\rangle_{\text{imp}}, \tag{C36}$$

where $\mathcal{V}_{\mathbf{k}'}$ is the momentum space volume. In this analysis we consider the Edwards model with the Gaussian white noise approximation for the impurity potential. Then, under this condition we can find that $\langle V^2_{\mathbf{k},\mathbf{k}'}\rangle_{\text{imp}} = V_{\text{imp}}$ is a constant that only depends on the material. Therefore, we can conclude our final expression for the inverse scattering time matrix as

$$\left(\frac{1}{\tau(\varepsilon,\mathbf{k})}\right)^{nn'}_{\alpha\beta} = \frac{2\pi V_{\text{imp}}}{\hbar}\frac{1}{\mathcal{V}_{\mathbf{k}'}}\sum_{\mathbf{k}'}\sum_\gamma c^n_{\alpha\gamma}(\mathbf{k},\mathbf{k}') \times \left[c^{n'}_{\beta\gamma}(\mathbf{k},\mathbf{k}')\right]^*\delta[\varepsilon - \varepsilon_\gamma(\mathbf{k}')]. \tag{C37}$$

APPENDIX D: DRESSING FIELD EFFECTS ON SPP WAVELENGTH AND DECAY LENGTHS

First, we take into account the dressing field effects on the SPP wavelength. Then, we introduce the normalized SPP wavelength as

$$\Lambda = \frac{\lambda_{\text{spp}}}{\lambda} = \sqrt{\frac{1+\epsilon'_2}{\epsilon'_2}}. \tag{D1}$$

Using the normalized energy band broadening or damping effect in the dressed metal $\chi = \varsigma/\varsigma_0$ in Eq. (45), we rewrite the normalized SPP wavelength

$$\Lambda = \sqrt{\frac{2\Omega^2 + 2\chi^2\varsigma_0^2 - \Omega_p^2}{\Omega^2 + \chi^2\varsigma_0^2 - \Omega_p^2}}. \tag{D2}$$

For better understanding, we can define the normalized SPP wavelength difference factor

$$\tilde{\Lambda} = \frac{\Lambda - \Lambda|_{\chi=1}}{\Lambda|_{\chi=1}}, \tag{D3}$$

where $\Lambda|_{\chi=1}$ represents the natural normalized wavelength of SPP. The relationship between $\tilde{\Lambda}$ and χ is plotted in Fig. 10

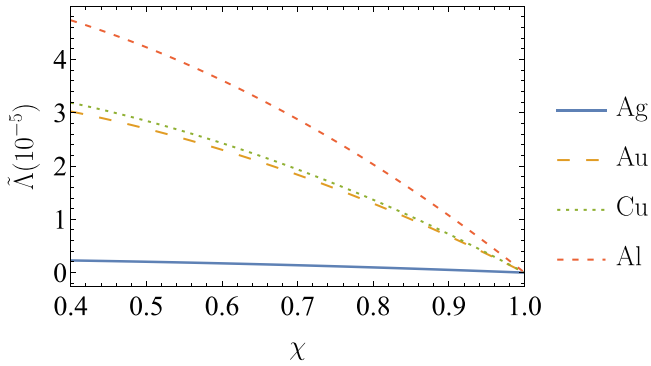

FIG. 10. The normalized SPP wavelength Λ against the normalized energy band broadening χ for Ag, Au, Cu, and Al. The empirical material parameters for the metals are obtained from Refs. [90,96,97].

for Ag, Au, Cu, and Al. All four metals show a positive-valued normalized difference factor against the normalized damping factor. In other words, the wavelength of the dressed SPP increases with reducing the total energy band broadening. It can be observed from Fig. 10 that the behavior and shape of Au curves look like those of Cu, whereas Ag-based curves show a significant reluctance against the modification of the normalized damping factor. Moreover, Al shows a bit higher alteration compared to the other three metals. It is important

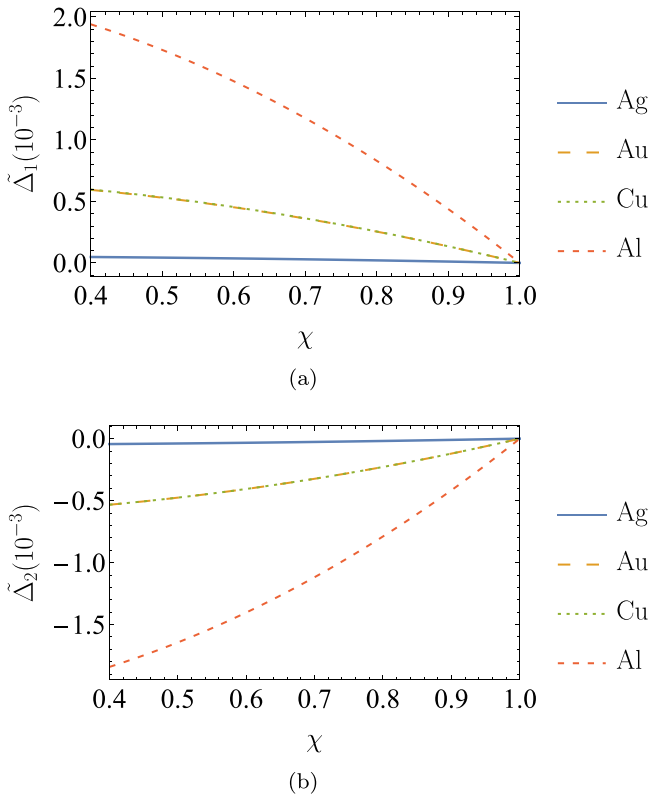

FIG. 11. The normalized SPP decay length Δ_j in (a) air ($j = 1$) and (b) metal ($j = 2$) against the normalized energy band broadening χ for Ag, Au, Cu, and Al. The empirical material parameters for the metals are obtained from Refs. [90,96,97].

to notice that these changes induced by the dressing field is of the order of a tenth of an angstrom.

Next, we focus on the decay length of electric fields of SPP. The electric field of the SPP decays when they move away from the interface. Using the expression in Eq. (53), and only considering the first-order terms of $|\epsilon_2''|/|\epsilon_2'|$, we derive expressions for the normal component of the wave number in the region of air

$$\varrho_{z,1} = \frac{\Omega}{c}\sqrt{\frac{1}{1+\varepsilon_2'}}\left[1 - i\frac{\varepsilon_2''}{2(1+\varepsilon_2')}\right], \tag{D4}$$

and the mettalic region

$$\varrho_{z,2} = \frac{\Omega}{c}\sqrt{\frac{\varepsilon_2'^2}{1+\varepsilon_2'}}\left[1 + i\frac{\varepsilon_2''}{2\varepsilon_2'}\right]. \tag{D5}$$

Then, we write the decay length for the two regions ($j = 1, 2$) as

$$\delta_j = \frac{1}{2\varrho_{z,j}''}, \tag{D6}$$

and define the normalized decay length by

$$\Delta_j = \frac{\delta_j}{\lambda}. \tag{D7}$$

Finally, we can identify the normalized decay length the two regions

$$\Delta_j = \frac{1}{2\lambda \mathrm{Im}(\varrho_{z,j})}. \tag{D8}$$

Further, we introduce the normalized decay length difference factor as

$$\tilde{\Delta}_j = \frac{\Delta_j - \Delta_j|_{\chi=1}}{\Delta_j|_{\chi=1}}, \tag{D9}$$

where $\Delta_j|_{\chi=1}$ represents the natural normalized decay length of SPP. The variation of $\tilde{\Delta}_j$ in air and metal regions against χ are shown in the subfigures of Fig. 11. Here, we can observe that the normalized decay length in the air $\tilde{\Delta}_1$ shows a positive-valued difference factor while the normalized decay length in the metal $\tilde{\Delta}_2$ shows a negative-valued difference factor for all four metals. This implies that with lower values of χ, the decay length of SPP in the air tends to increase while it gets decreases inside the metal region. Additionally, Au-based curves behave similarly to Cu, and Ag demonstrate a very low deviation against the variation of χ compared to other metals. The decay length of Al-based SPP shows bit higher change compared to other metals in both regions. However, these changes in decay lengths in both regions are an order of an angstrom in the best cases.

[1] D. K. Gramotnev and S. I. Bozhevolnyi, Nat. Photonics **4**, 83 (2010).
[2] R. Zia, J. A. Schuller, A. Chandran, and M. L. Brongersma, Mater. Today **9**, 20 (2006).
[3] D. A. Miller, in *Device Research Conference. Conference Digest (Cat. No. 01TH8561)* (IEEE, New York, 2001).
[4] M. Born and E. Wolf, *Principles of Optics: Electromagnetic Theory of Propagation, Interference, and Diffraction of Light* (Elsevier, Amsterdam, 2013).
[5] J. Takahara and T. Kobayashi, Opt. Photonics News **15**, 54 (2004).
[6] M. L. Brongersma and V. M. Shalaev, Science **328**, 440 (2010).
[7] W. L. Barnes, A. Dereux, and T. W. Ebbesen, Nature (London) **424**, 824 (2003).
[8] D. Pines, Rev. Mod. Phys. **28**, 184 (1956).
[9] R. H. Ritchie, Phys. Rev. **106**, 874 (1957).
[10] C. J. Powell and J. B. Swan, Phys. Rev. **115**, 869 (1959).
[11] E. A. Stern and R. A. Ferrell, Phys. Rev. **120**, 130 (1960).
[12] D. Sarid and W. A. Challener, *Modern Introduction to Surface Plasmons: Theory, Mathematica Modeling, and Applications* (Cambridge University Press, Cambridge, England, 2010).
[13] M. Premaratne and M. I. Stockman, Adv. Opt. Photon. **9**, 79 (2017).
[14] X. Fan, W. Zheng, and D. J. Singh, Light Sci. Appl. **3**, e179 (2014).
[15] T. Warnakula, S. D. Gunapala, M. I. Stockman, and M. Premaratne, Phys. Rev. B **100**, 085439 (2019).
[16] T. Attanayake, M. Premaratne, and G. P. Agrawal, Plasmonics **10**, 1453 (2015).
[17] K. Shimanoe, S. Endo, T. Matsuyama, K. Wada, and K. Okamoto, Sci. Rep. **11**, 5169 (2021).
[18] H. Oka and Y. Ohdaira, Sci. Rep. **8**, 2643 (2018).
[19] T. Perera, S. Mallawaarachchi, and M. Premaratne, J. Phys. Chem. Lett. **12**, 11214 (2021).
[20] M. G. Blaber, M. D. Arnold, and M. J. Ford, J. Phys. Chem. C **113**, 3041 (2009).
[21] T. Perera, S. D. Gunapala, M. I. Stockman, and M. Premaratne, J. Phys. Chem. C **124**, 27694 (2020).
[22] D. Sikdar, W. Cheng, and M. Premaratne, J. Appl. Phys. **117**, 083101 (2015).
[23] H. B. Jeon, P. V. Tsalu, and J. W. Ha, Sci. Rep. **9**, 1 (2019).
[24] W. Xiong, D. Sikdar, M. Walsh, K. J. Si, Y. Tang, Y. Chen, R. Mazid, M. Weyland, I. D. Rukhlenko, J. Etheridge, M. Premaratne, X. Li, and W. Cheng, Chem. Commun. **49**, 9630 (2013).
[25] J. Cao, T. Sun, and K. T. Grattan, Sens. Actuators B Chem. **195**, 332 (2014).
[26] Y. Liu, T. Perera, Q. Shi, Z. Yong, S. Mallawaarachchi, B. Fan, J. Walker, C. Lupton, S. Thang, M. Premaratne *et al.*, Nanoscale **14**, 4292 (2022).
[27] K. C. Ng, I. B. Udagedara, I. D. Rukhlenko, Y. Chen, Y. Tang, M. Premaratne, and W. Cheng, ACS Nano **6**, 925 (2012).
[28] K. J. Si, D. Sikdar, Y. Chen, F. Eftekhari, Z. Xu, Y. Tang, W. Xiong, P. Guo, S. Zhang, Y. Lu *et al.*, ACS Nano **8**, 11086 (2014).
[29] E. N. Economou, Phys. Rev. **182**, 539 (1969).
[30] J. J. Burke, G. I. Stegeman, and T. Tamir, Phys. Rev. B **33**, 5186 (1986).
[31] S. Wedge and W. L. Barnes, Opt. Express **12**, 3673 (2004).
[32] J. Takahara, S. Yamagishi, H. Taki, A. Morimoto, and T. Kobayashi, Opt. Lett. **22**, 475 (1997).
[33] V. A. Podolskiy, A. K. Sarychev, E. E. Narimanov, and V. M. Shalaev, J. Opt. A: Pure Appl. Opt. **7**, S32 (2005).
[34] K. Leosson, T. Nikolajsen, A. Boltasseva, and S. I. Bozhevolnyi, Opt. Express **14**, 314 (2006).
[35] J. Jung, T. Søndergaard, and S. I. Bozhevolnyi, Phys. Rev. B **76**, 035434 (2007).
[36] B. Wang and G. P. Wang, Opt. Lett. **29**, 1992 (2004).
[37] S. A. Maier, Opt. Commun. **258**, 295 (2006).
[38] D. F. Pile, T. Ogawa, D. Gramotnev, T. Okamoto, M. Haraguchi, M. Fukui, and S. Matsuo, Appl. Phys. Lett. **87**, 061106 (2005).
[39] E. Moreno, F. Garcia-Vidal, S. G. Rodrigo, L. Martin-Moreno, and S. I. Bozhevolnyi, Opt. Lett. **31**, 3447 (2006).
[40] A. Boltasseva, V. S. Volkov, R. B. Nielsen, E. Moreno, S. G. Rodrigo, and S. I. Bozhevolnyi, Opt. Express **16**, 5252 (2008).
[41] M. Quinten, A. Leitner, J. R. Krenn, and F. R. Aussenegg, Opt. Lett. **23**, 1331 (1998).
[42] S. A. Maier, P. G. Kik, H. A. Atwater, S. Meltzer, E. Harel, B. E. Koel, and A. A. Requicha, Nat. Mater. **2**, 229 (2003).
[43] W. H. Weber and G. W. Ford, Phys. Rev. B **70**, 125429 (2004).
[44] J. Homola, Chem. Rev. **108**, 462 (2008).
[45] A. G. Brolo, Nat. Photonics **6**, 709 (2012).
[46] T. Nikolajsen, K. Leosson, and S. I. Bozhevolnyi, Appl. Phys. Lett. **85**, 5833 (2004).
[47] M. J. Dicken, L. A. Sweatlock, D. Pacifici, H. J. Lezec, K. Bhattacharya, and H. A. Atwater, Nano Lett. **8**, 4048 (2008).
[48] T. W. Ebbesen, C. Genet, and S. I. Bozhevolnyi, Phys. Today **61**(5), 44 (2008).
[49] J. Chen, Z. Li, S. Yue, and Q. Gong, Nano Lett. **11**, 2933 (2011).
[50] J. Chen, Z. Li, X. Zhang, J. Xiao, and Q. Gong, Sci. Rep. **3**, 1451 (2013).
[51] M. Mansuripur, A. R. Zakharian, A. Lesuffleur, S.-H. Oh, R. J. Jones, N. C. Lindquist, H. Im, A. Kobyakov, and J. V. Moloney, Opt. Express **17**, 14001 (2009).
[52] D. O'Connor, M. McCurry, B. Lafferty, and A. V. Zayats, Appl. Phys. Lett. **95**, 171112 (2009).
[53] T. D. Heidel, J. K. Mapel, M. Singh, K. Celebi, and M. A. Baldo, Appl. Phys. Lett. **91**, 093506 (2007).
[54] P. Prabhathan and V. M. Murukeshan, Plasmonics **11**, 253 (2016).
[55] D. Handapangoda, M. Premaratne, I. D. Rukhlenko, and C. Jagadish, Opt. Express **19**, 16058 (2011).
[56] D. Handapangoda, I. D. Rukhlenko, and M. Premaratne, J. Opt. Soc. Am. B **29**, 553 (2012).
[57] W. Zhu, I. D. Rukhlenko, and M. Premaratne, J. Opt. Soc. Am. B **29**, 2659 (2012).
[58] D. Handapangoda, I. D. Rukhlenko, and M. Premaratne, J. Opt. **15**, 035006 (2013).
[59] K. Leosson, J. Nanophoton. **6**, 061801 (2012).
[60] W. Zhu, I. D. Rukhlenko, and M. Premaratne, Appl. Phys. Lett. **101**, 031907 (2012).
[61] T. Wijesinghe, M. Premaratne, and G. P. Agrawal, Opt. Express **22**, 2681 (2014).
[62] D. J. Bergman and M. I. Stockman, Phys. Rev. Lett. **90**, 027402 (2003).
[63] C. Jayasekara, M. Premaratne, S. D. Gunapala, and M. I. Stockman, J. Appl. Phys. **119**, 133101 (2016).

[64] M. I. Stockman, J. Opt. **12**, 024004 (2010).
[65] B. Liu, W. Zhu, S. D. Gunapala, M. I. Stockman, and M. Premaratne, ACS Nano **11**, 12573 (2017).
[66] T. Oka and S. Kitamura, Annu. Rev. Condens. Matter Phys. **10**, 387 (2019).
[67] M. Polini, F. Guinea, M. Lewenstein, H. C. Manoharan, and V. Pellegrini, Nat. Nanotechnol. **8**, 625 (2013).
[68] M. C. Rechtsman, J. M. Zeuner, Y. Plotnik, Y. Lumer, D. Podolsky, F. Dreisow, S. Nolte, M. Segev, and A. Szameit, Nature (London) **496**, 196 (2013).
[69] M. Kleber, Phys. Rep. **236**, 331 (1994).
[70] M. Grifoni and P. Hänggi, Phys. Rep. **304**, 229 (1998).
[71] N. Goldman and J. Dalibard, Phys. Rev. X **4**, 031027 (2014).
[72] A. A. Pervishko, O. V. Kibis, S. Morina, and I. A. Shelykh, Phys. Rev. B **92**, 205403 (2015).
[73] S. Morina, O. V. Kibis, A. A. Pervishko, and I. A. Shelykh, Phys. Rev. B **91**, 155312 (2015).
[74] M. Wackerl, P. Wenk, and J. Schliemann, Phys. Rev. B **101**, 184204 (2020).
[75] A. Eckardt, Rev. Mod. Phys. **89**, 011004 (2017).
[76] K. Herath and M. Premaratne, Phys. Rev. B **105**, 035430 (2022).
[77] G. Floquet, in *Sur les équations différentielles linéaires á coefficients périodiques*, Annales scientifiques de l'École Normale Supérieure, Serie 2, Vol. 12 (Elsevier, 1983), pp. 47–88.
[78] M. Holthaus, J. Phys. B: At. Mol. Opt. Phys. **49**, 013001 (2016).
[79] O. V. Kibis, Europhys. Lett. **107**, 57003 (2014).
[80] K. Dini, O. V. Kibis, and I. A. Shelykh, Phys. Rev. B **93**, 235411 (2016).
[81] M. S. Rudner and N. H. Lindner, Nat. Rev. Phys. **2**, 229 (2020).
[82] K. I. Seetharam, C.-E. Bardyn, N. H. Lindner, M. S. Rudner, and G. Refael, Phys. Rev. X **5**, 041050 (2015).
[83] S. A. Weidinger and M. Knap, Sci. Rep. **7**, 45382 (2017).
[84] K. I. Seetharam, C.-E. Bardyn, N. H. Lindner, M. S. Rudner, and G. Refael, Phys. Rev. B **99**, 014307 (2019).
[85] S. G. Lee, P. A. Harten, J. P. Sokoloff, R. Jin, B. Fluegel, K. E. Meissner, C. L. Chuang, R. Binder, S. W. Koch, G. Khitrova, H. M. Gibbs, N. Peyghambarian, J. N. Polky, and G. A. Pubanz, Phys. Rev. B **43**, 1719 (1991).
[86] M. Joffre, D. Hulin, A. Migus, A. Antonetti, C. B. à La Guillaume, N. Peyghambarian, M. Lindberg, and S. Koch, Opt. Lett. **13**, 276 (1988).
[87] E. Akkermans and G. Montambaux, *Mesoscopic Physics of Electrons and Photons* (Cambridge University Press, Cambridge, England, 2007).
[88] H. Bruus and K. Flensberg, *Many-Body Quantum Theory in Condensed Matter Physics: An Introduction* (Oxford University Press, Oxford, 2004).
[89] P. B. Crilly, A. B. Carlson, and J. C. Rutledge, Communication Systems (McGraw-Hill, New York, 2009).
[90] S. O. Kasap, *Principles of Electronic Materials and Devices*, Vol. 2, (McGraw-Hill, New York, 2006).
[91] G. Dattoli, L. Giannessi, L. Mezi, and A. Torre, Il Nuovo Cimento B **105**, 327 (1990).
[92] S. Harris and O. McDuff, IEEE J. Quantum Electron. **1**, 245 (1965).
[93] A. E. Siegman, *Lasers* (University Science Books, Sausalito, CA, 1986).
[94] S. Longhi and P. Laporta, Phys. Rev. A **60**, 4016 (1999).
[95] R. E. Hummel, *Electronic Properties of Materials* (Springer Science & Business Media, New York, 2011).
[96] N. Ashcroft and N. Mermin, *Solid State Physics* (Cengage Learning, Boston, 2011).
[97] P. R. West, S. Ishii, G. V. Naik, N. K. Emani, V. M. Shalaev, and A. Boltasseva, Laser Photonics Rev. **4**, 795 (2010).
[98] L. Novotny and B. Hecht, *Principles of Nanooptics* (Cambridge University Press, Cambridge, England, 2012).
[99] M. Premaratne and G. P. Agrawal, *Theoretical Foundations of Nanoscale Quantum Devices* (Cambridge University Press, Cambridge, England, 2021).
[100] P. B. Johnson and R. W. Christy, Phys. Rev. B **6**, 4370 (1972).
[101] See Supplemental Material at http://link.aps.org/supplemental/10.1103/PhysRevB.106.235422 for complete numerical simulations of the dressed SPP characteristics.
[102] D. H. Dunlap and V. M. Kenkre, Phys. Rev. B **34**, 3625 (1986).
[103] A. Endo, N. Hatano, H. Nakamura, and R. Shirasaki, J. Phys.: Condens. Matter **21**, 345803 (2009).
[104] T. Bilitewski and N. R. Cooper, Phys. Rev. A **91**, 033601 (2015).
[105] H. Hapuarachchi, S. Mallawaarachchi, H. T. Hattori, W. Zhu, and M. Premaratne, J. Phys.: Condens. Matter **30**, 054006 (2018).
[106] Y. Zhang, K. Aslan, M. J. Previte, and C. D. Geddes, Appl. Phys. Lett. **90**, 173116 (2007).
[107] M. J. Previte, Y. Zhang, K. Aslan, and C. D. Geddes, Appl. Phys. Lett. **91**, 151902 (2007).
[108] K. Okamoto, I. Niki, A. Shvartser, Y. Narukawa, T. Mukai, and A. Scherer, Nat. Mater. **3**, 601 (2004).
[109] Q. Zhang, G. Li, X. Liu, F. Qian, Y. Li, T. C. Sum, C. M. Lieber, and Q. Xiong, Nat. Commun. **5**, 4953 (2014).
[110] R. Buckley and P. Berini, Opt. Express **15**, 12174 (2007).
[111] J. Gosciniak, T. Holmgaard, and S. I. Bozhevolnyi, J. Light. Technol. **29**, 1473 (2011).
[112] Z. Han and S. I. Bozhevolnyi, Rep. Prog. Phys. **76**, 016402 (2013).
[113] M. Noginov, V. A. Podolskiy, G. Zhu, M. Mayy, M. Bahoura, J. Adegoke, B. Ritzo, and K. Reynolds, Opt. Express **16**, 1385 (2008).
[114] J. Seidel, S. Grafström, and L. Eng, Phys. Rev. Lett. **94**, 177401 (2005).
[115] D. Y. Fedyanin, A. V. Krasavin, A. V. Arsenin, and A. V. Zayats, Nano Lett. **12**, 2459 (2012).
[116] M. Ambati, S. H. Nam, E. Ulin-Avila, D. A. Genov, G. Bartal, and X. Zhang, Nano Lett. **8**, 3998 (2008).
[117] J. Grandidier, G. C. Des Francs, S. Massenot, A. Bouhelier, L. Markey, J.-C. Weeber, C. Finot, and A. Dereux, Nano Lett. **9**, 2935 (2009).
[118] R. Zia, M. D. Selker, and M. L. Brongersma, Phys. Rev. B **71**, 165431 (2005).
[119] S. I. Bozhevolnyi, J. Erland, K. Leosson, P. M. W. Skovgaard, and J. M. Hvam, Phys. Rev. Lett. **86**, 3008 (2001).
[120] B. Wang and G. P. Wang, Appl. Phys. Lett. **87**, 013107 (2005).
[121] K. Tanaka and M. Tanaka, Appl. Phys. Lett. **82**, 1158 (2003).
[122] T. Holmgaard and S. I. Bozhevolnyi, Phys. Rev. B **75**, 245405 (2007).
[123] A. S. Baburin, A. S. Kalmykov, R. V. Kirtaev, D. V. Negrov, D. O. Moskalev, I. A. Ryzhikov, P. N. Melentiev, I. A.

Rodionov, and V. I. Balykin, Opt. Mater. Express **8**, 3254 (2018).
[124] P. N. Melentiev, A. A. Kuzin, and V. I. Balykin, Quantum Electron. **47**, 266 (2017).
[125] I. Radko, S. I. Bozhevolnyi, G. Brucoli, L. Martín-Moreno, F. García-Vidal, and A. Boltasseva, Opt. Express **17**, 7228 (2009).
[126] A. Evlyukhin, S. Bozhevolnyi, A. Stepanov, R. Kiyan, C. Reinhardt, S. Passinger, and B. Chichkov, Opt. Express **15**, 16667 (2007).
[127] L. Tong, H. Wei, S. Zhang, and H. Xu, Sensors **14**, 7959 (2014).
[128] H. Wei, S. Zhang, X. Tian, and H. Xu, Proc. Natl. Acad. Sci. **110**, 4494 (2013).
[129] Y. Wan, Z. Zheng, Z. Lu, J. Liu, and J. Zhu, Sens. Actuators B Chem. **162**, 35 (2012).
[130] H. Yoon, K. Y. Yeung, P. Kim, and D. Ham, Philos. Trans. R. Soc. A **372**, 20130104 (2014).
[131] T. N. Ikeda and A. Polkovnikov, Phys. Rev. B **104**, 134308 (2021).
[132] T. Mori, Floquet States in Open Quantum Systems, arXiv:2203.16358.
[133] D. M. Wolkow, Z. Phys. **94**, 250 (1935).
[134] L. V. Keldysh *et al.*, Sov. Phys. JETP **20**, 1307 (1965).
[135] N. K. Rahman, Phys. Rev. A **10**, 440 (1974).
[136] H. D. Jones and H. R. Reiss, Phys. Rev. B **16**, 2466 (1977).
[137] R. Xu, D. Zhang, A. Kheifets, and I. Ivanov, arXiv:1411.5550.
[138] D. Kidd, C. Covington, Y. Li, and K. Varga, Phys. Rev. B **97**, 024303 (2018).
[139] D. J. Griffiths and D. F. Schroeter, *Introduction to Quantum Mechanics* (Cambridge University Press, Cambridge, England, 2018).
[140] W. C. Henneberger, Phys. Rev. Lett. **21**, 838 (1968).
[141] J.-P. Connerade, *Highly Excited Atoms*, Vol. 9 (Cambridge University Press, Cambridge, England, 1998).
[142] M. Wackerl, Transport in Periodically Driven Systems, Ph.D. thesis, University of Regensburg, 2020.
[143] S. F. Edwards, Philos. Mag. **3**, 1020 (1958).
[144] J. Rammer, *Quantum Transport Theory* (CRC Press, Boca Raton, FL, 2018).
[145] G. D. Mahan, *Many-Particle Physics* (Springer Science & Business Media, New York, 2000).